Mechanical Behavior of Porcelain

BY

Max C. Modugno

A THESIS
SUBMITTED TO THE FACULTY OF

ALFRED UNIVERSITY

IN PARTIAL FULFILLMENT OF THE REQUIREMENTS
FOR THE DEGREE OF

MASTER OF SCIENCE

IN

CERAMIC ENGINEERING

ALFRED, NEW YORK

January, 2021

Mechanical Behavior of Porcelain

BY

Max C. Modugno

B.S. Alfred University 2015

SIGNATURE OF AUTHOR_____

APPROVED BY_____

DR. WILLIAM M. CARTY, ADVISOR

_____

DR. WILLIAM C. LACOURSE, ADVISORY COMMITTEE

_____

DR. WILLIAM CARLSON, ADVISORY COMMITTEE

_____

CHAIR, ORAL THESIS DEFENSE

ACCEPTED BY_____

GABRIEL GASTAUD, DEAN
KAZUO INAMORI SCHOOL OF ENGINEERING

ACKNOWLEDGMENTS

I would like to first thank the folks at Victor Insulator, especially Gary Leshkivich and Kyle Norsen, for providing materials and time to make this work possible. I will miss the life lessons Gary taught me over lunch at Finn's Tapp Room.

I have been fortunate to have two amazing mentors in the world of ceramics: Dr. William Carty and Dr. Andrew Wereszczak. As I was failing out of the ceramic engineering program during my sophomore year, Dr. Carty gave me an opportunity to work in his lab. The hands-on experience I gain led to a drastic improvement in my academics. He also introduced me to my second mentor, Dr. Wereszczak, who provided me with an opportunity to spend two years working at Oak Ridge National Laboratory and introducing me to the southern lifestyle. Dr. Wereszczak has taught me everything I know about mechanical test and properties of brittle materials and provided valuable insight throughout this researcher.

Finally, I would like to thank my parents, Lenore and Felix Modugno. They have provided me with the moral values to get to this point in my life.

TABLE OF CONTENTS

LIST OF TABLES

Page

LIST OF FIGURES

Page

ABSTRACT

Several theories have been proposed to describe the mechanical behavior of porcelains, all of which suggest that the behavior of porcelain is inconsistent with brittle failure theories. The literature demonstrates that the mechanical properties of porcelains are frequently measured without the measurement of elastic properties. When the elastic modulus and fracture surface energy are incorporated into the strength data analysis, porcelains behave in a perfectly brittle manner, indicating that the proposed theories describing the mechanical behavior are unnecessary. This work shows a direct correlation between stress at failure and elastic modulus of quartz and alumina porcelains with a uniform flaw population. Weibull statistics along with fractography indicate a single flaw population of quartz grains at the tensile surface ranging between 50 and 80 μm for both porcelain bodies consistent with the calculated flaw size. Real time age effects on strengths were found to be non-existent and cyclic exposure to high-pressure steam caused unglazed test specimen to significantly increase in strength. All findings indicate porcelains behave in a classic linear elastic manner.

I. INTRODUCTION

A. Mechanical Properties of Porcelains

Three theories have been presented to describe the strengths of porcelains that, in essence, imply brittle fracture criteria does not apply.[1] The mullite theory was presented by Zoellner in 1908 suggesting mullite levels were directly related to the strength of porcelains.[2] His initial conclusion was drawn by looking at mullite content of Berlin and Seger porcelains which had different compositions and heat treatments. The stronger Berlin porcelain happened to have higher mullite levels leading to the first theory describing strengths of porcelain.

The mullite theory was later revised to state that both the mullite content and the degree of interlocking mullite grains controlled the strength.[3] It was proposed that small interlocking needles reinforced the glass matrix.

In 1918 Gilchrest and Klinefelter showed increasing quartz content led to a higher strength porcelain body.[4] This led to the matrix-reinforcement hypothesis which suggests the difference in coefficient of thermal expansion between the matrix and dispersed particles leaded to a compressive stress in the matrix. Size limits were placed on the quartz particles for matrix-reinforcing by Warshaw and Seider.[5] They found that highest strength porcelains required quartz particle smaller than 25 μm. However, Pinto found no strength benefits in using quartz particle smaller than 25 μm.[6]

Researchers have shown that adding higher strength dispersed particles such as alumina increase the strength of porcelains leading to the dispersion-strengthening theory.[7,8] It is suggested that the dispersed particles limit the critical flaw population thus creating a stronger body. What is missing in this argument is the significant increase in elastic modulus associated with the incorporation of alumina.

It has been proposed that porcelains weaken with age.[9-13] The β- to α-quartz inversion at 573°C on cooling has been blamed for generating microcracks in the glass phase due to the large volumetric contraction in the quartz particle. One group used acoustic emission spectroscopy to look for evidence of microcracking; however, no signal was detected at the quartz inversion temperature.[14] Evidence for glass phase microcracking

typically come from electron images of polished and etched microstructures.[9-11] Both of these preparation steps can lead to deterioration of the glass matrix surrounding quartz grains due to residual tensile strain from differences is the coefficient of thermal expansion (CTE). This has led to the belief that slow crack growth occurs causing degradation over time.[12,13] It is important to also note that over-etching of porcelain microstructures presented in the literature, polished examples shown in Figure. 1, lead to incorrect generalizations regarding the role of quartz in porcelains.

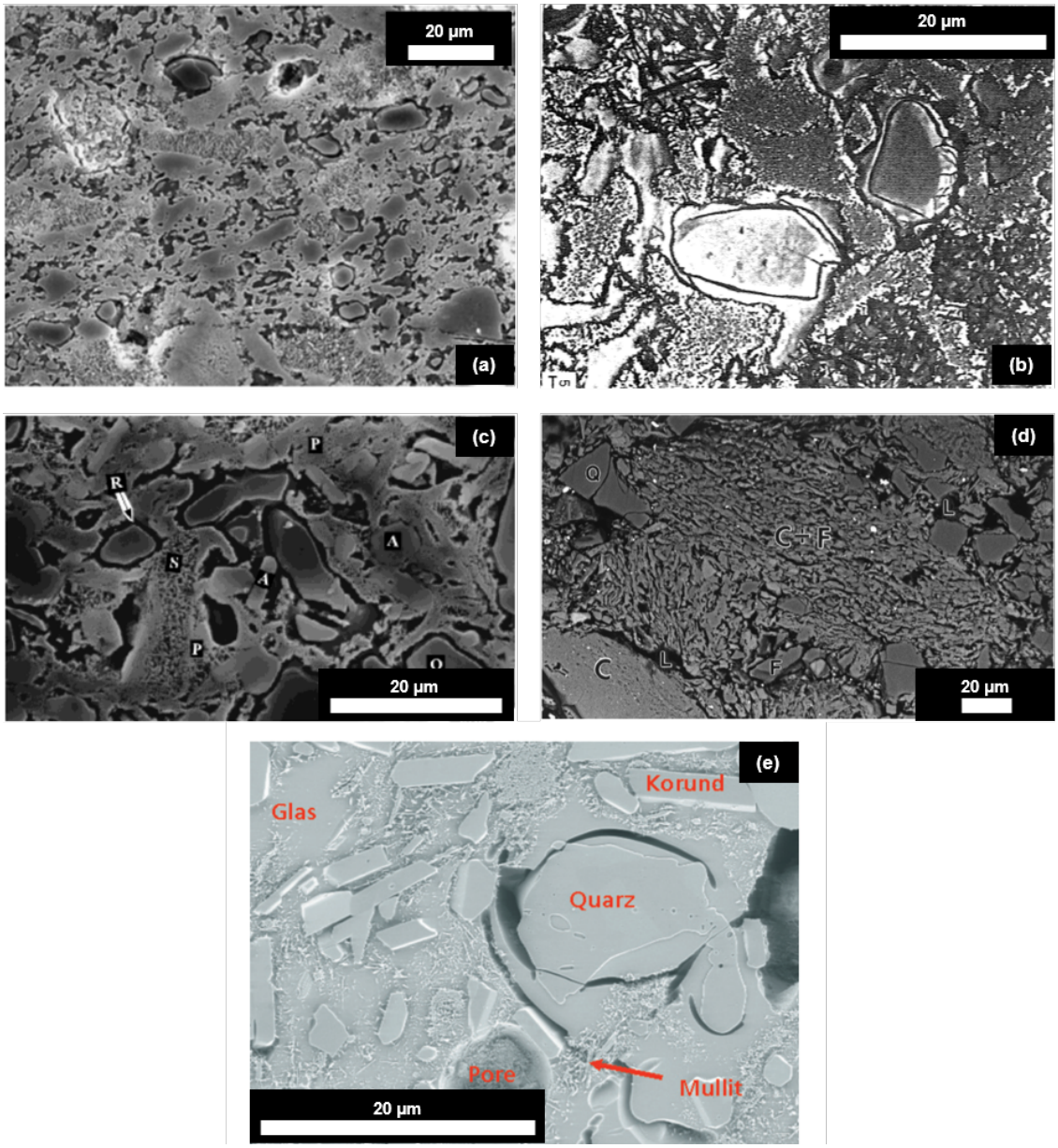

Figure 1. Examples of over-etched microstructure in literature of (a) sanitary ware porcelain,[15] (b) quartz porcelain,[16] (c) quartz porcelain,[17] (d) triaxial porcelain,[18] and (e) aluminous electrical porcelain.[9]

B. Mechanical Testing of Brittle Materials

Brittle materials always fail due to tensile stress. The three main tests for brittle materials are: uniaxial tensile, 3-point bending, and 4-point bending, as illustrated schematically in Figure 2.

Uniaxial testing is simply pulling a sample along a single axis. This allows for the greatest volume to be tested. However, due to the geometry of the test, samples must be gripped, locally concentrating stresses at the grip locations. To avoid defects introduced by gripping, dog-bone shaped samples are typically made which require machining of samples resulting in possible defects.[19,20]

Flexural testing (also refer to as bend testing) is conducted using three or four points of contact. A 3-point bend test has two lower supports for the specimen to rest on. A third upper support center loads the sample between the two lower supports creating two equal moments. This generates a maximum tensile stress at the surface directly below the upper support (center load point). Since the probability of strength limiting flaw being at the point of highest stress is unlikely, overall stress at failures tend to be slightly higher than the results obtained from 4-point bending.[21]

A larger volume of a specimen is tested when four points of contact are used. Therefore, the likelihood of the largest flaw causing failure is increased resulting in statistically lower strengths. This results in 4-point bend testing configuration being preferred because of the larger volume tested and the ease of implementation.

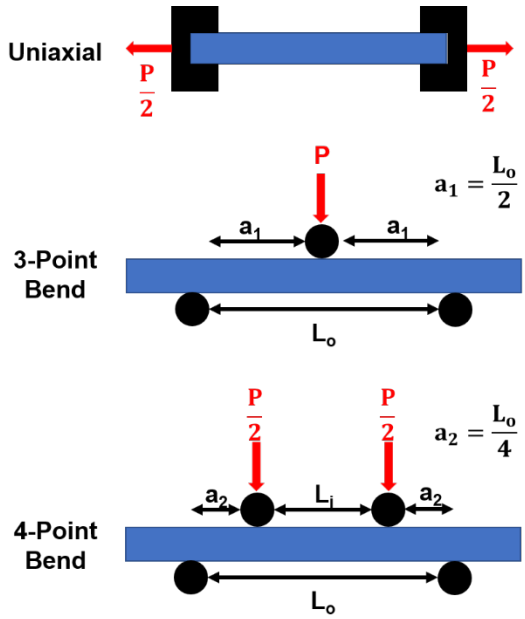

Figure 2. Various loading configurations used to determine strength of brittle materials.

Test specimen geometry can also contribute to the test results. Two typical geometries are common: circular cross section rods or rectangular cross section bars. Bars are preferred since a larger effective volume is tested. Rods are preferred for extrusion testing as fabrication defects are relatively easy to avoid. The curvature of the rod, however, generates a high stress intensity at the tensile rod surface concentrating the stress in a small volume. This is less favorable since it poorly represents the test specimen.

In this work, the rod and bar geometries were combined to increase the tested volume while eliminating fabrication defect generation. A novel oval shape was developed (Figure 3) that presents a large, flat region with minimal stress intensity issues.

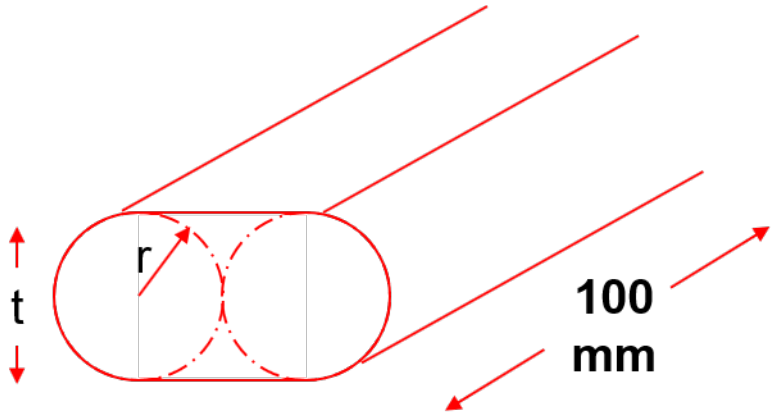

Figure 3. Cross-section of novel bend bar design shown schematically.

Loading rate can contribute to the data in systems that have the potential for interaction with the environment, specifically those containing a glassy component. In glass containing samples, a slow loading rate can promote slow crack growth resulting in apparently weaker samples, although the high chemical durability of the porcelain glass makes this unlikely.[20] Fast loading rates can generate apparently higher strengths. A standard method, using a rate of 1 mm/s, has been universally adapted as an ideal loading rate condition regardless of specimen geometry.[22]

C. Fractography

Fractographic techniques use fracture surface markings to identify the crack direction and potentially the fracture origin. This is a crucial step for the analysis of failure mechanisms thus allowing for engineering changes to be applied to enhance the mechanical properties.

Key fracture marking used to determine failure origins include fracture mirrors, mist hackle, velocity hackle (as shown in Figure 4). Fracture origins are centered in the fracture mirror. The mirror is a smooth region on the fracture surface generated by the initial propagation of the crack front. As the crack velocity approaches critical velocity, the fracture surface becomes rough generating a region known as mist hackle. Once the critical velocity has been reached, the hackle becomes coarse. Hackle can also be formed as the crack front propagates through an internal pore generating a wake.

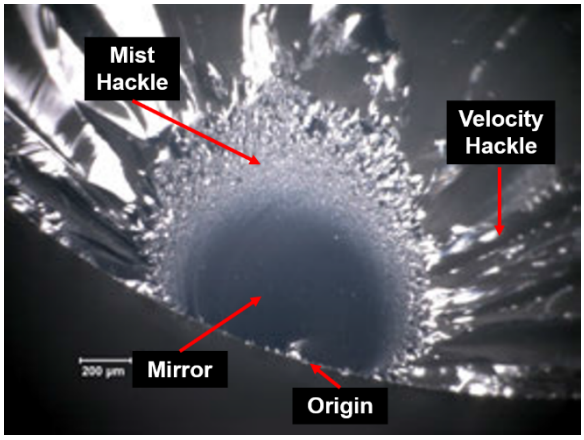

Figure 4. Fracture markings used to determine cause of failure.

D. Weibull Statistics

A two parameter Weibull distributions is typically used to describe the failures of brittle materials. The shape of this distribution is a skewed normal distribution where the maximum frequency occurs at 63.2% rather than 50% emphasizing the low end of a data set. Therefore, the characteristic strength of a material fitting a Weibull distribution is defined as the strength when the probability of failure is 63.2%.

The Weibull distribution for a dataset is determined from Equation 1 utilizing the probability of failure (PF) which is defined in Equation 2.

$$WD = Ln(Ln(\frac{1}{1-PF})) \quad (1)$$

$$PF = \frac{n-0.5}{N} \quad (2)$$

Where n is the specimen ranking and N is the total number of test specimen. A Weibull plot is generated by plotting the natural logarithm of the stress at failure against the Weibull distribution.

A Weibull plot is a useful tool for evaluation of flaw populations. A schematic of an ideal Weibull distribution can be seen in Figure 5. The monomodal behavior associated with a line of a single slope (the Weibull modulus) indicates a single flaw population. The steeper the slope (or higher the Weibull modulus), the narrower the flaw population and the smaller the stress window for failure. Since failure of brittle materials are related to defects introduced in processing, a steeper slope also indicates a more robust process and a narrower flaw population.[23,24]

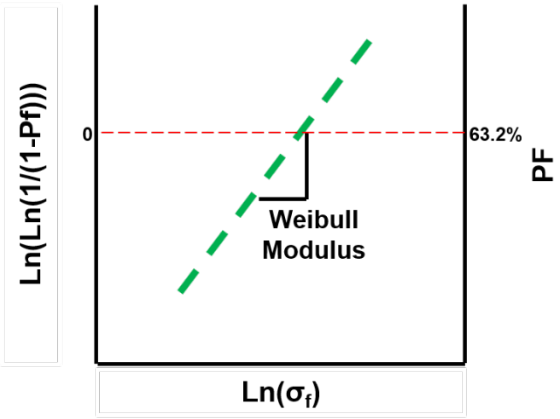

Figure 5. Example of a Weibull plot showing an ideal distribution of strengths.

In the design of brittle materials, the weakest sample establishes the design criteria. Weibull distributions are commonly used tools for designing a product that must satisfy

specific mechanical loads. The Weibull data can be extrapolated to determine the probability of failure for a given mechanical load condition.

Weibull distributions can also provide insight into multiple flaw populations (i.e. inclusions, internal pores, surface defects) or issues with processing and testing (specimen processed on different days, variations in processing, testing under different conditions…). Figure 6 shows two possible bimodal distributions. When high strength populations have a larger modulus, or narrower distribution, compared to the low strength, or wide distribution of stress at failure, then a concurrent flaw population exists. This indicates that there are two sets of flaw types present (concurrent) in the set of specimens, for example, surface defects and internal pores.

Exclusive flaw populations can be identified when the low strength population has a higher modulus (steeper slope) than the high strength population. Exclusivity suggests that there were inconsistencies with the processing of the sample, such as samples heat treated in different furnaces, or that during testing different test conditions were used, such as a change in loading rate or misalignment of mechanical test fixture.

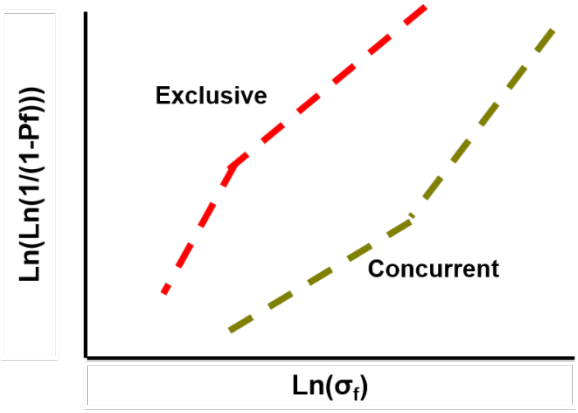

Figure 6. Schematic showing concurrent and exclusive flaw populations

II. EXPERIMENTAL PROCEDURE

A. Sample Preperation

All test specimens were obtained from industrially prepared high-tension electrical porcelain.*

1. Extrusion

Test specimen were prepared via extrusion of slurry processed filter pressed plastic porcelain bodies. Bodies used were quartz and alumina porcelains consisting of kaolin, feldspar, quartz and corundum. An industrial vacuum extruder with a deairing chamber using a high-density polyethylene die onto a lubricated (Kroil™, Kano Laboratories Inc, Nashville, TN) steel plate. Extrudates were placed on a flat dust-free surface to dry overnight followed by Victor's standard 24-hr drying process utilizing excess heat from the tunnel kiln.

2. Glazing

Green test specimen hung from 5 mm (0.2 inch) diameter alumina rods, then dipped into production glaze (SG8E Large Post Glaze, Victor Insulators Inc., Victor, NY). A submersion time of eight seconds was used to obtain the desired glaze thickness. The alumina rods with 10 specimens per rod were then spanned between silicon carbide (SiC) beams on a kiln car to dry prior to firing.

---

* Victor Insulators, Victor, NY. Standard factory compositions for quartz and alumina porcelains. The test specimens were produced on-site and heat treated in production facilities.

3. Firing

A single fire heat treatment was conducted in an industrial tunnel kiln. Green bars were laid flat on cordierite kiln selves coated with alumina. The surface in contact with the lubricated steel plate during extrusion was in contact with the kiln wash during firing. This provided a defect and contaminant free (top) surface for mechanical testing. Figure 7 shows a loaded kiln car prior to entering the tunnel kiln.

All specimens fit on two kiln cars. The cars travelled through the tunnel kiln over the course of three days. A trace of the heating cycle is shown in Figure 8. The general cycle was heating at a rate of 0.5 K/minute to a peak temperature of 1249°C (2280°F) with a five-hour dwell and then cooled at an average rate of 0.65 K/minute to room temperature. Note the decreased cooling rate around the quartz transitions temperature at 573°C. This is commonly implemented in industry to minimize residual strain, however, once below the glass transition temperature, the cooling rate will have no effect on the resulting strain from the rapid volumetric contraction associated with the β-quartz to α-quartz inversion.

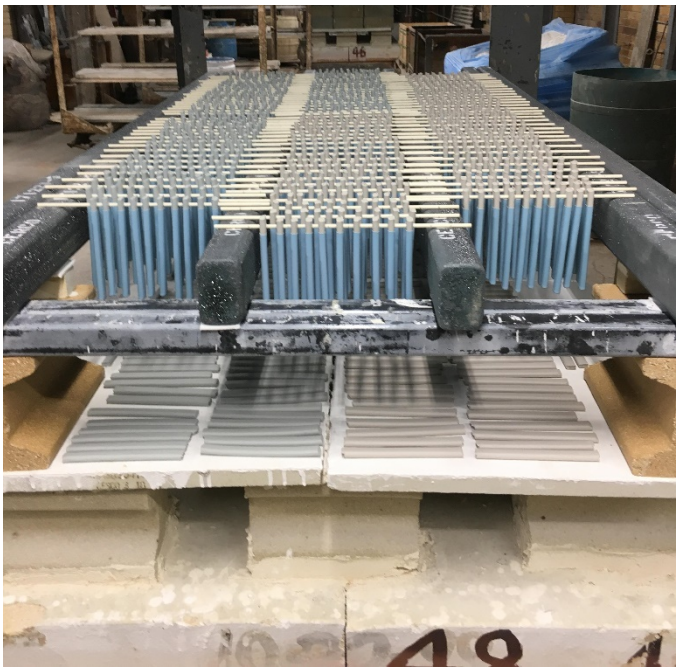

Figure 7. Photograph of kiln car prior to entering tunnel kiln. Unglazed bend bars can be seen laying across kiln washed refractory. Glazed bend bars can be seen suspended from alumina rods and spanned across SiC beams.

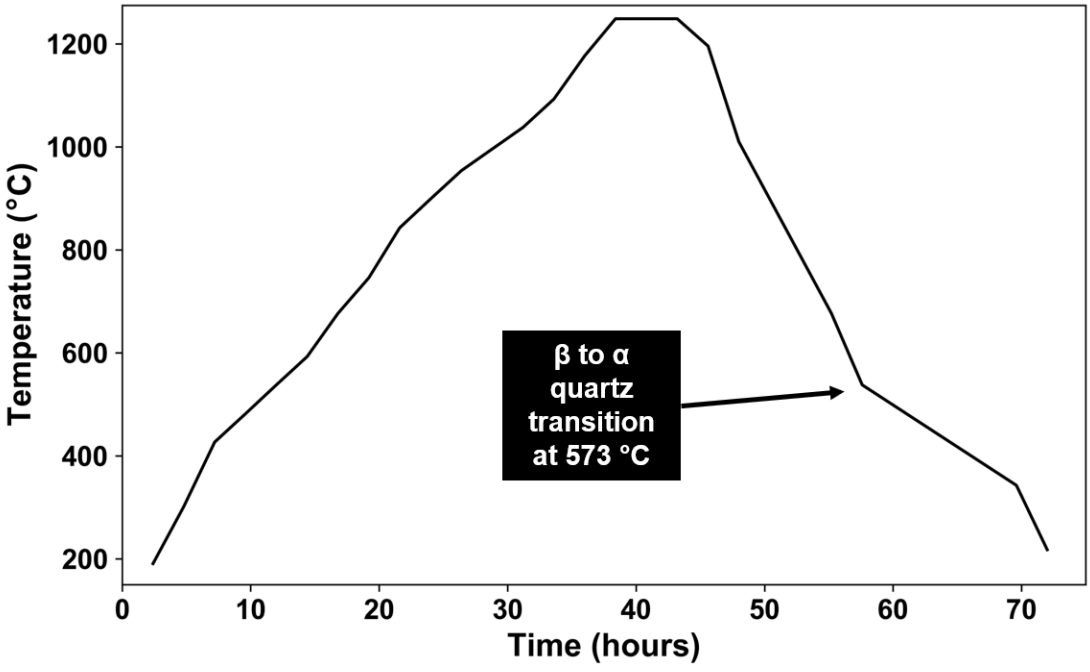

Figure 8. Temperature profile of three-day heat treatment.

B. Characterization

1. Chemical Composition of the Porcelain Bodies

Chemical composition of the two porcelain bodies is presented in Table I and were determined with inductively coupled plasma – atomic emission spectroscopy (ICP-AES, Bureau Veritas Minerals, Vancouver, Canada).

Table I. Chemical composition of quartz and alumina porcelain determined with ICP-AES.

Oxide	Quartz Body (mass %)	Alumina Body (mass %)	Quartz Body (mole %)	Alumina Body (mole %)
SiO_2	67.95	43.55	77.82	56.41
Al_2O_3	24.92	50.05	16.82	38.21
Na_2O	0.31	0.27	0.34	0.34
K_2O	4.82	4.02	3.52	3.32
MgO	0.14	0.14	0.23	0.26
CaO	0.16	0.15	0.19	0.20
SrO	0.02	0.02	0.01	0.01
BaO	0.12	0.11	0.05	0.05
Fe_2O_3	0.71	0.91	0.30	0.45
TiO_2	0.78	0.73	0.66	0.71
ZrO_2	0.03	0.02	0.01	0.01
P_2O_5	0.05	0.03	0.03	0.02

2. Mineralogy

Using an internal standard quantitative x-ray diffraction (QXRD) method, mineralogy was determined. Powder samples were prepared by grinding the porcelain bodies to below 44 μm (sub-325 mesh) with an auto-mortar/pestle. 10 mass % calcium

fluoride (CaF_2) was added as an internal standard then ground an additional ten minutes to mix.

Diffraction patterns (Figure 9) of back-loaded powder samples were collected with a diffractometer (D2 Phaser, Bruker, Germany) utilizing copper Kα radiation (λ=1.54 Å). Patterns were collected from 15 to 60° 2θ with a 0.04° 2θ step size and a four second count time. Analysis software (Jade, v.9, Materials Data Inc., Livermore, CA, USA) was used to determine peak areas of three non-overlapping peaks (Table II) per mineral phase. Peak areas are compared to three CaF_2 peaks to determine quantitative mineralogical values based on a previously generated calibration curve (Table III).[25,26] Note that mineralogical values assume no porosity in the fired bodies.

Table II. Mineral phases and respective Bragg reflections used for quantitative analysis.

Mineral Phase	Bragg Reflection	Peak Position (°2θ)	PDF Number
Corundum	(110) (220) (121)	37.8, 43.3, 52.5	01-075-1865
Mullite	(001) (220) (121)	30.9, 33.2, 40.8	01-079-1455
Quartz	(110) (111) (112)	20.8, 40.3, 50.1	00-046-1045
Fluorite	(111) (220) (331)	28.2, 47.0, 55.7	00-035-0816

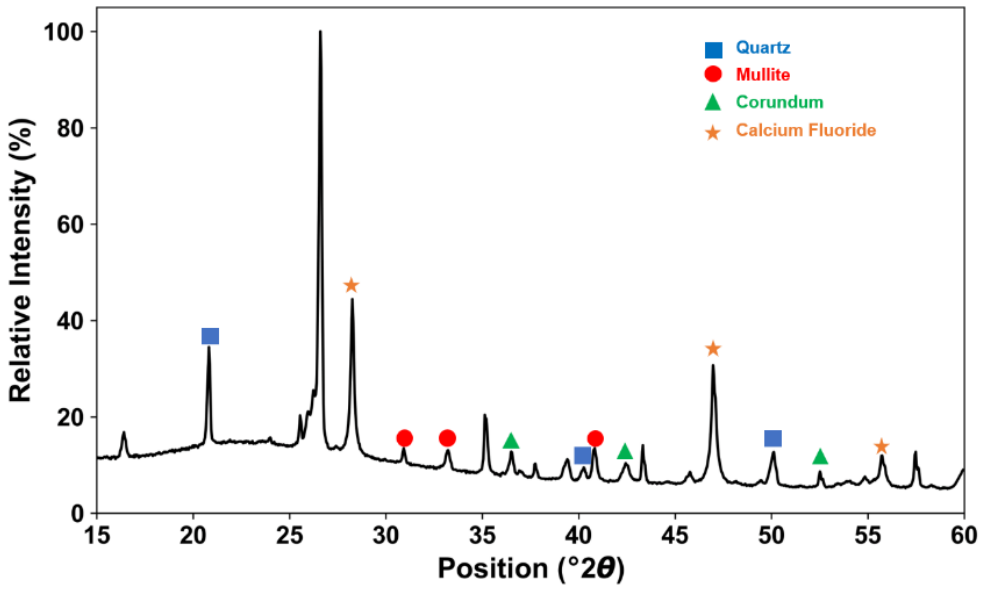

Figure 9. Diffraction pattern of quartz porcelain showing non-overlapping peaks used for quantitative analysis.

Table III. Measured mineralogy of porcelains.

	Mineralogy (wt%)			
	Quartz	Mullite	Corundum	Glass
Quartz Porcelain	18.03	18.57	6.72	56.69
Alumina Porcelain	8.07	6.01	37.89	48.03

3. Glass Phase Composition

The glass phase composition was determined by subtracting the measured mineral content determined via QXRD from the measured body chemistry. Resulting chemistries are reported in Table IV on a mass, molar and unity molecular formula (UMF) basis.

Table IV. Chemistry of glass phases in quartz and alumina porcelains determined with QXRD and ICP-AES.

Chemical	Quartz Body Glass Phase (mass %)	Alumina Body Glass Phase (mass %)	Quartz Body Glass Phase (mole %)	Alumina Body Glass Phase (mole %)	UMF Quartz porcelain glass	UMF Alumina porcelain glass
SiO_2	78.83	73.41	74.35	58.68	11.93	11.11
Al_2O_3	8.58	13.26	4.77	6.25	0.77	1.18
Na_2O	0.54	0.57	0.49	0.44	0.08	0.08
K_2O	8.51	8.37	5.12	4.27	0.82	0.81
MgO	0.24	0.28	0.34	0.34	0.05	0.06
CaO	0.28	0.31	0.28	0.26	0.05	0.05
SrO	0.03	0.03	0.02	0.02	0.00	0.00
BaO	0.21	0.22	0.08	0.69	0.01	0.01
Fe_2O_3	1.25	1.90	0.44	0.57	0.07	0.11
TiO_2	1.38	1.53	0.97	0.91	0.16	0.17
ZrO_2	0.05	0.05	0.01	0.01	0.00	0.00
P_2O_5	0.09	0.07	0.04	0.02	0.01	0.00

4. Apparent Bulk Density

Apparent bulk density (ρ_{app}) and water absorption of the two porcelain compositions were determined using a standard method modified for small specimen sizes by measuring to the nearest 0.1 mg.[27] Resulting values are presented in Table V.

Table V. Apparent bulk density and water adsorption of quartz and alumina porcelain.

Composition	ρ_{app} ($g.cm^{-3}$)	Water Adsorption (%)
Quartz Porcelain	2.457 ±0.022	0.04 ±0.01
Alumina Porcelain	2.7632 ±0.0003	0.05 ±0.03

5. Elastic Modulus

Two methods, displacive and acoustic, were used to determine the elastic modulus of the porcelain bodies and compared to calculated elastic modulus from rule of mixture (ROM).

Displacive measurements were performed by analyzing the load-displacement data during flexural testing by conversion to stress-strain values consistent with the test specimen geometry.[19,20,22] The tensile strain, ε, is calculated from the cross-head displacement, y, using Equation 3.

$$\varepsilon = \frac{6yD}{L_o^2} \tag{3}$$

where D is the thickness of the bend bar, and L_o is the outer span of the test fixture.[22]

The crosshead displacement must be corrected by subtracting out the compliance of the system. This is accomplished by loading an "infinitely" stiff material, in this case a bar of tungsten carbide, and monitoring the displacement behavior. A calibration curve is generated from the loaded-displacement behavior and applied to the crosshead displacement collected for the porcelains. An example of load-displacement curves for the raw data, instrument compliance and corrected data are presented in Figure 10.

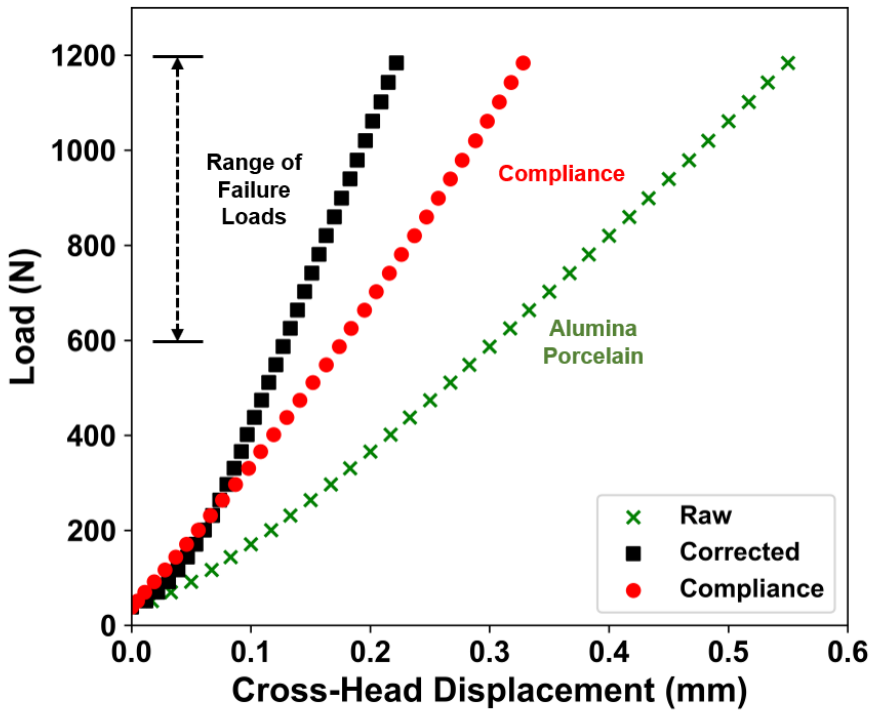

Figure 10. Load-displacement relationships of raw data, instrument compliance and the corrected data obtain by subtracting instrument compliance from raw load-displacement behavior.

The acoustic method for determining the elastic modulus uses a technique commonly referred to as the pulse-echo technique. Poisson's ratio, ν, and elastic modulus, E, are obtained by determining the velocity of acoustic waveforms through a material in accordance with a standard method.[12] Samples for the velocity measurements were prepared by cutting ~8 mm thick sections of a 1" diameter rod with a low speed diamond saw. Thickness of the sample was used to determine the velocity of the acoustic wave in the material. Transverse (v156, Olympus IMS, Tokyo, Japan) and longitudinal (v110, Olympus IMS, Tokyo, Japan) transducers were coupled to the sample with honey, then acoustic waves were applied. Waveforms were analyzed with an oscilloscope to determine

the transverse and longitudinal velocities (Equation 4). The Poisson ratio was calculated using Equation 5.

$$V_T = \frac{P_T}{t}, V_L = \frac{P_L}{t} \tag{4}$$

$$\nu = \frac{1-2(\frac{V_T}{V_L})^2}{2-2(\frac{V_T}{V_L})^2} \tag{5}$$

where V_T and V_L are the transverse and longitudinal velocities, respectively, P_T and P_L are the transverse and longitudinal times per pulse, respectively, and t is the sample thickness. The resulting Poisson ratio, along with the apparent bulk density (ρ) and the longitudinal velocity, were used to determine the elastic modulus (E) using Equation 6.

$$E = V_L^2 \rho \frac{(1+\nu)(1-2\nu)}{1-\nu} \tag{6}$$

Rule of mixtures (ROM) was applied to calculate the elastic modulus of the porcelain systems by assuming that the elastic modulus is equal to the sum of the volume fractions (F_V) of each component with M, Q, G, C and P represent mullite, quartz, glass, corundum and porosity, respectively (Equation 7). Table VI shows the densities and elastic moduli of the four components in porcelain bodies along with the volume fractions making up the two bodies used in this study. Note that these values differ from those present in Table III due to the introduction of void space in the material.

$$E = F_{M,V}E_M + F_{Q,V}E_Q + F_{G,V}E_G + F_{C,V}E_C + F_{P,V}E_P \tag{7}$$

Table VI. Volume fraction of constituents making up porcelain bodies and respective densities and elastic moduli.[6]

Material	Quartz Body (Vol%)	Alumina Body (Vol%)	ρ ($g.cm^{-3}$)	E (GPa)
Mullite	14.8	6.4	3.15	150
Quartz	17.2	5.5	2.65	94
Glass	61.1	56.8	2.42	70
Corundum	3.7	26.9	3.95	390
Void Space	3.4	4.4	--	--

6. Glaze Chemistry

The UMF, also known as the Seger formula, was used to characterize the glaze based on its chemistry. Table VII shows the resulting UMF of the glaze used in this study.

Table VII. Unity molecular formula of glaze applied to test specimen.

Constituent	SiO_2	Al_2O_3	Na_2O	K_2O	CaO	MgO
UMF	4.59	0.52	0.05	0.09	0.77	0.08

C. Test Specimen Design

A novel bend bar was designed to minimize extrusion defects such as edge tearing. This was accomplished by altering a standard test specimen geometry for flexural strength testing.[22]

The stress state for this geometry can be described by the standard relationship shown in Equation 8.

$$\sigma = \frac{Mc}{I}, \tag{8}$$

where M is the applied moment, c is the distance from the neutral axis to the surface or half the specimen thickness (t), and I is the moment of inertia (MOI) of the geometry.[20] The MOI can be delineated as the sum of a circle with a radius equal to half the geometry thickness and a square with sides equal to the thickness (Figure 11) leading to Equation 9. Equation 10 defines the MOI for a square (I_s) and a circle (I_c).[28]

$$I = I_s + \frac{2I_c}{2} \tag{9}$$

$$I_s = \frac{t^4}{12} \quad I_c = \frac{\pi(\frac{t}{2})^4}{4} \tag{10}$$

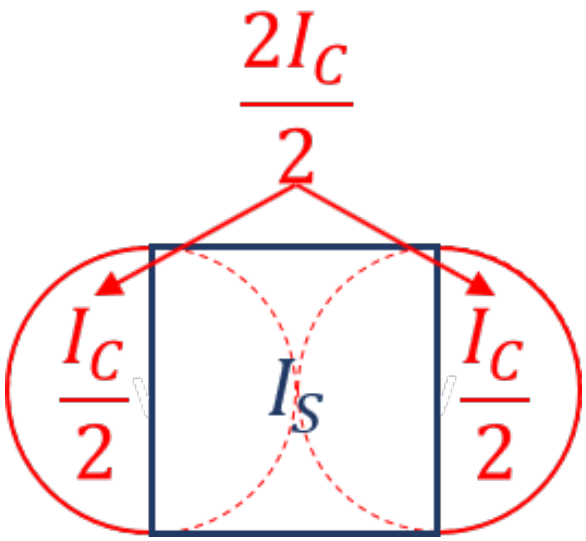

Figure 11. Cross section of specimen showing square and circular MOI.

The applied moment is dependent on the loading configuration during testing. In this study a 4-point bend configuration (Figure 12) will be used resulting in Equation 11:

$$M = \frac{PL_o}{8} \tag{11}$$

where P is the applied load and L_o is the length of the lower span.

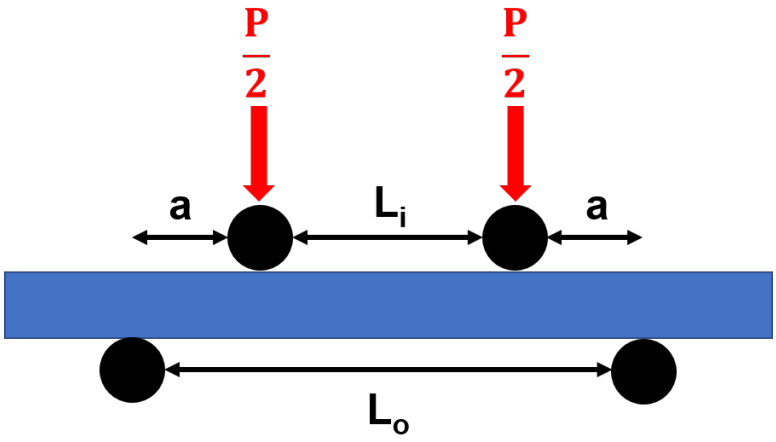

Figure 12. Loading configuration used for flexural testing.

Substituting Equation 9 and Equation 11 into Equation 8 results in Equation 12 describing the stress at failure for the novel test geometry.

$$\sigma_f = \frac{24P_f(L-b)}{(2+3\pi)h^3} = \frac{48P_f a}{(2+3\pi)h^3} \quad (12)$$

Where P_f and t_f are, respectively, the load in newtons and thickness at failure in meters resulting in stress values in pascals.

A lower and upper span of 80 and 40 mm, respectively, create an effective volume of approximately 2.5 cm^3 being tested.

A loading rate of 1 mm/min utilizing a mechanical test frame (Model 5566, Instron Company, Norwood, Massachusetts) equipped with a 10 kN loadcell was used to determine the load at failure. A fully articulated fixture ensured loading normal to the specimen surface in accordance with a standard test method.[22]

D. Fractography

Fractography was conducted using both stereo microscopy and scanning electron microscopy (SEM). Optical microscopy aided in identifying the failure origins. Samples were illuminated with a goose neck external light source at a low illumination angle allowing for better resolution of the fracture surfaces. Critical flaw types were determined by analyzing SEM images.

E. Critical Flaw Size Calculations

Griffith's theory was applied to calculate the critical flaws size using Equation 13.[29]

$$c = \frac{2E\gamma}{\pi\sigma_f^2} \tag{13}$$

Where E is the elastic modulus, γ is the surface energy, and σ_f is the stress at failure. This assumes an elliptical initial flaw shape and that the crack propagates when adequate energy in the form of elastic strain is provided sufficient to generate two new (fracture) surfaces.[14] Elastic moduli determined acoustically were used for the calculations and the fracture surface energies were determined using a novel technique based on crazing of glazes on the bodies.[30]

F. Aging

Samples are aging to investigate the mechanical behavior of porcelain over the course of 30 years. Conditions mimic those seen by high-tension electrical insulators in service, meaning they are exposed to natural weather conditions. The samples are being aged in western New York, therefore, they are exposed to broadly changing temperatures, rain, snow, and (occasionally) sunshine. Bend bars are planned to be tested on a log-time

scale as outlined in Table VIII. A statistically relevant dataset will be obtained by collecting 30 datapoints for each decade allowing for complete Weibull analysis.[24]

Table VIII. Ages of test specimen being tested, and the corresponding number of test specimens being tested.

Age (Years)		0.01	0.03	0.1	0.3	1	3	10	30
Testing Date	Date	4/13	4/21	5/16	8/3	4/10	4/9	4/7	4/2
	Year	2018	2018	2018	2018	2019	2021	2028	2048
Sample Size		30	20	30	20	30	30	30	30

G. Aging in the Presence of Steam

A separate aging study was conducted evaluating the effect of high-pressure steam, applied using an autoclave, on mechanical behavior. It is widely accepted that autoclaving accelerates the aging process, but it is not clear if this is globally true. In the autoclave, test specimens were placed onto an elevated platform within the autoclave chamber with approximately one liter of deionized water in the bottom of the chamber. The chamber was sealed then heated using a machine-controlled process to generate high pressure steam.

The samples were autoclaved in cycles. Each cycle included a ramp up to the desired pressure, an hour soak at pressure, followed by venting of the chamber back to atmospheric pressure. A sample size of 30 specimens were tested per condition.

III. RESULTS AND DISCUSSION

A. Microstructures – Determination of Etching Conditions

To analyze the porcelain microstructures, etching conditions were evaluated qualitatively by observing effects of hydrofluoric acid (HF) concentration, duration of etch, and solution temperature on the features visible in quartz and alumina porcelains. Test specimens were polished to a 1 μm finish then etched using a combination of the parameters shown in Table IX. Samples were carbon coated and imaged using a scanning electron microscope (Quanta 200 ESEM, FEI Company, Hillsboro, OR).

Table IX. Test conditions used to evaluate etching conditions.

HF Concentration	5, 10, 20 wt%
Exposure Time	10, 20 sec
Solution Temperature	0, 20 °C

Effects of time are shown in Figure 13 and 14 for polished quartz porcelain microstructures. Substantial differences are not seen with respect to exposure time and solution temperature, however, HF concentration was found to be the most important variable on etching porcelain. Using a weak 5 wt% solution, minor etching of the glass phase was seen making it difficult to resolve microstructural features. However, 20 wt% HF caused large craters to form in the microstructure. Ideal microstructures were found to result from using 10 wt% HF for 10 to 20 seconds. Microstructural features are easily identifiable from the preferential removal of the glass matrix without causing excessive damage and formation of craters in the glass matrix. Table X ranks the variables in terms of influence on etching. Note that cracking can be observed surrounding quartz grains, however, cracking is not present surrounding corundum grains. This difference can be attributed to CTE differences between quartz and corundum.

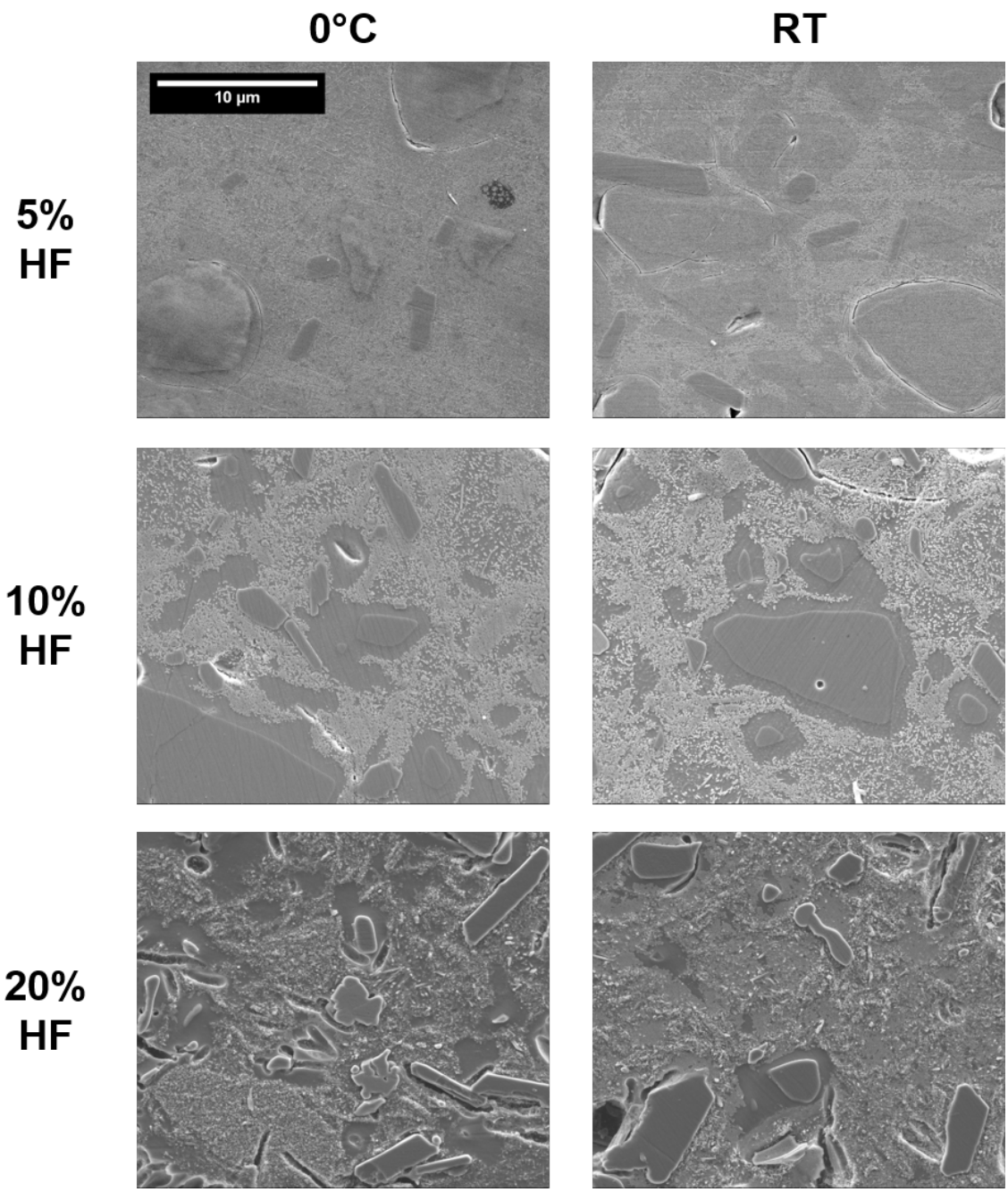

Figure 13. Quartz porcelain etched for 10 seconds at 0°C and room temperature (~20°C) in 5, 10 and 20 wt% HF solution.

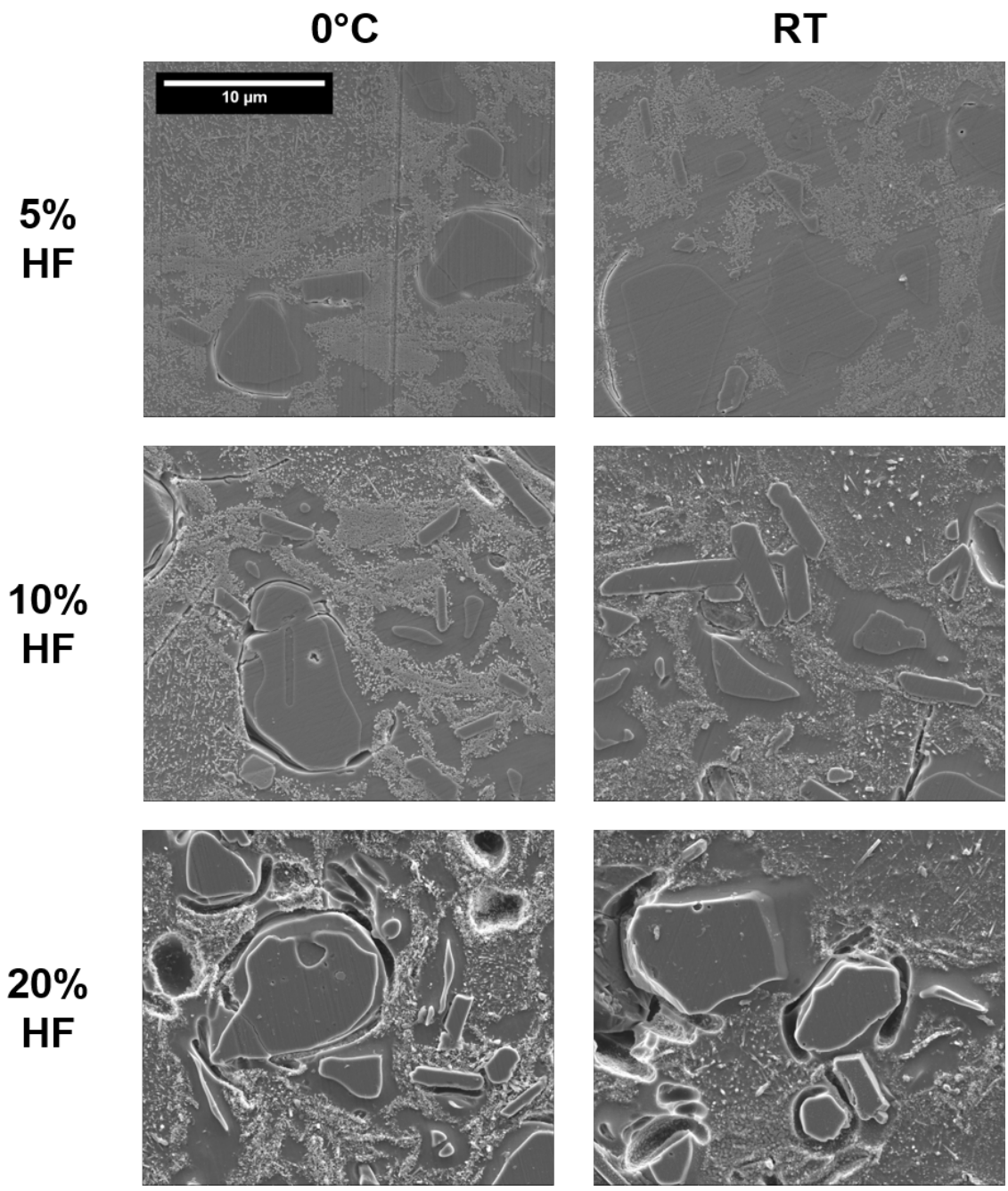

Figure 14. Quartz porcelain etched for 20 seconds at 0°C and room temperature (~20°C) in 5, 10 and 20 wt% HF solution.

Table X. Ranking of etching variables from most important (1) to least important (3).

Rank	Variable
1	HF Concentration
2	Immersion Time
3	Solution Temperature

Microstructures for quartz and alumina porcelains that had been etched with ideal conditions are shown in Figure 15. Both samples show the same constituents with the alumina porcelain having higher levels of corundum. Fine (primary) mullite needles form in clay relics whereas coarse (secondary) mullite evolves from feldspar. Note quartz dissolution rim surrounding quartz grains.

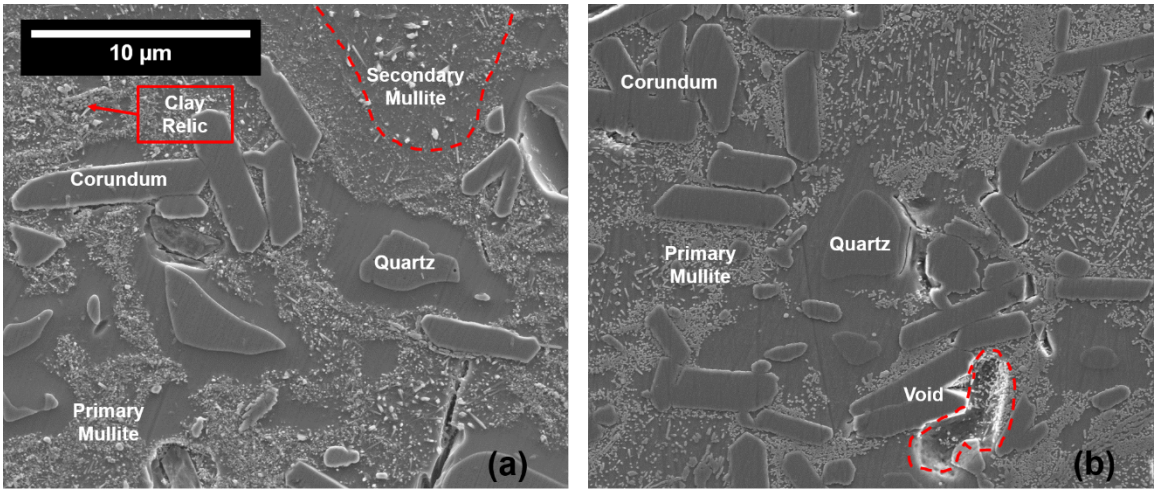

Figure 15. Microstructural features in (a) quartz and (b) alumina porcelains etched for 10 seconds in 10 wt% HF at room temperature.

B. Stress-Strain Relationships

The stress-strain relationship, corrected for compliance, of the porcelains tested show a classic linear elastic response excluding wind-up at low stresses (Fig. 16) which is an artifact of the elimination of slack in the testing fixtures. The initial stress at zero strain

is from pre-loading the test specimen to ~30 N to help remove slack from the system. This relationship is shown to be linear indicating linear-elastic behavior.

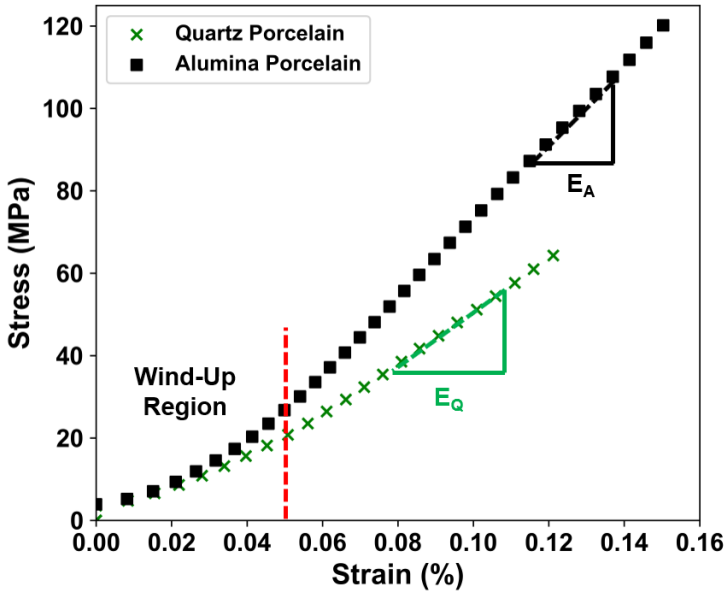

Figure 16. Stress-strain relationship for quartz and alumina porcelain showing linear elastic behavior

Failure criteria for brittle materials are directly related to the elastic modulus due to its relationship with fracture surface energy. However, elastic modulus is rarely discussed in relation to the strength of porcelains.[3,5,8] It has been demonstrated that strength scales linearly with elastic modulus directly effecting strengths of porcelains.[7]

Elastic moduli are tabulated in Table XI. Values obtained using the pulse-echo technique are in good agreement with the literature[7,23] and approximately 30% higher than those obtained by displacement. Pulse-echo elastic modulus, also referred to as zero-strain elastic modulus, values were used for strain at failure and critical flaw size calculations. Elastic modulus, E_o, are not reported for the glazed sample since the composite effects of the thin glaze layer have not been addressed.

Table XI. Elastic moduli and fracture surface energy of quartz and alumina porcelain.

Elastic Moduli (GPa)				Poisson's Ratio	Fracture Surface Energy (J/m^2)[6]
	Displacive (Finite)	Pulse-Echo (Zero-Strain)	ROM		
Quartz Porcelain	50.4	72.3	98.4	0.15	4.6
Alumina Porcelain	86.1	122.3	161.5	0.23	8.4

C. Real Time Aging

The distribution of the strength data was analyzed for normality qualitatively and quantitatively.[31] Figure 17 shows quartile-quartile (Q-Q) plots of 0.01 year strength data for the four material systems in this investigation. From a qualitative standpoint, the strength data appears to fit the expected normal distribution well. However, Table XII shows the results of two quantitative tests, a simple quantitative Wilks-Shapiro (w/s) test for normality[31] and a Jarque-Bera (JB) test[32] which determines skewedness and kurtosis. The w/s test suggests that the quartz and alumina porcelains follow a normal distribution, but when the shape of the strength distributions is considered, all fail the JB test. This suggests that an average and standard deviation can provide a reasonable first approximation, but a Weibull distribution better fits the datasets.

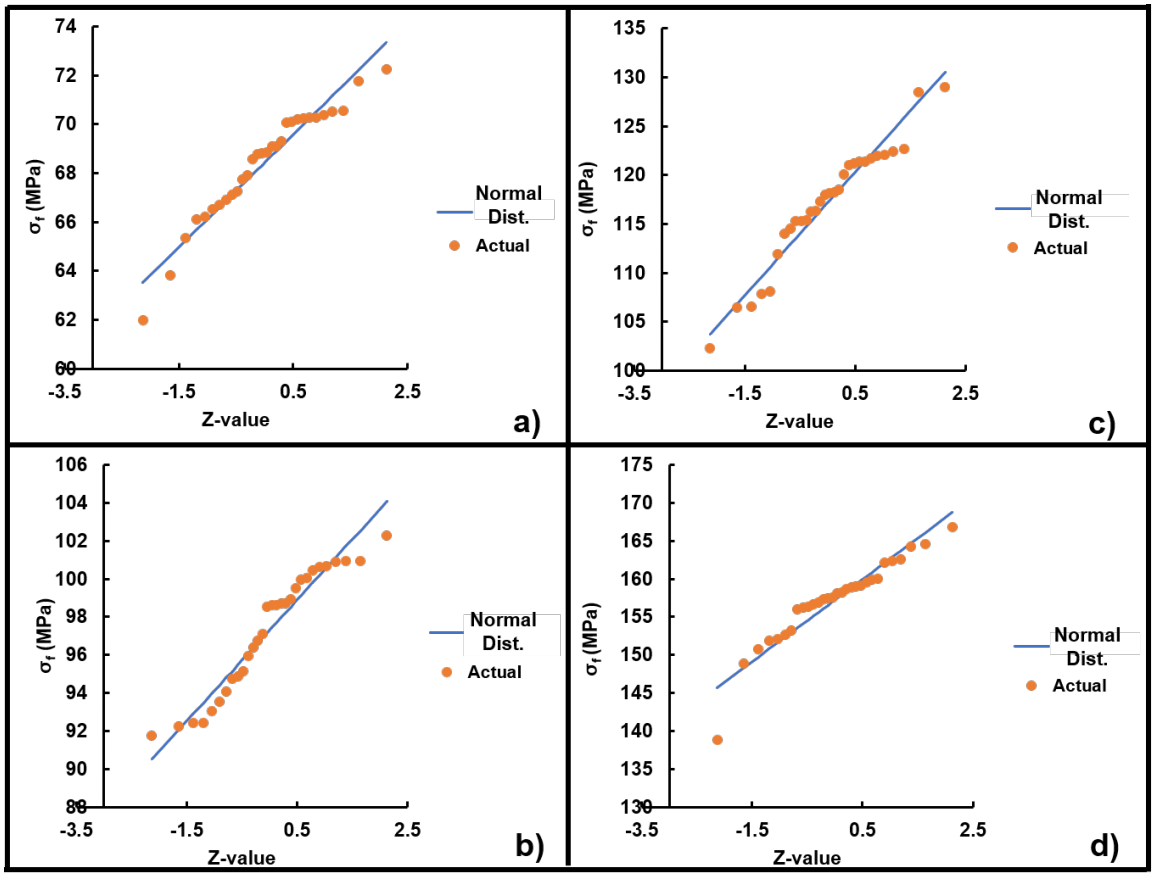

Figure 17. Q-Q plots showing normal distribution plotted against actual distribution of strength data for (a) quartz porcelain, (b) glazed quartz porcelain, (c) alumina porcelain, and (d) glazed alumina porcelain.

Table XII. Quantitative tests for normality based on 0.01 year strength datasets.

Dataset	Sample Size (n)	W/S Test Criteria[31]	W/S Result (Pass/Fail)	JB Criteria[32]	JB Test (Pass/Fail)
Quartz Porcelain	30	3.47<q<4.89	q=4.45 (Pass)	JB≤0.109	JB=3.03 (Fail)
Glazed Quartz Porcelain	30	3.47<q<4.89	q=3.31 (Fail)	JB≤0.109	JB=5.99 (Fail)
Alumina Porcelain	30	3.47<q<4.89	q=4.25 (Pass)	JB≤0.109	JB=1.05 (Fail)
Glazed Alumina Porcelain	30	3.47<q<4.89	q=5.16 (Fail)	JB≤0.109	JB=13.62 (Fail)

The compiled stress at failures plotted against a Weibull distribution are shown in Figure 18 for the four sample sets tested at 0.01, 0.03, 0.1 and 0.3 years. The Weibull moduli for each decade is reported for each test group. The alumina porcelain is approximately 45% stronger than the quartz porcelain which scales linearly with the difference in elastic modulus between the two systems. It is proposed that both porcelain bodies have the similar flaw populations since they were processed in the same manufacturing environment. The addition of glaze significantly increases the strength of both porcelain compositions.

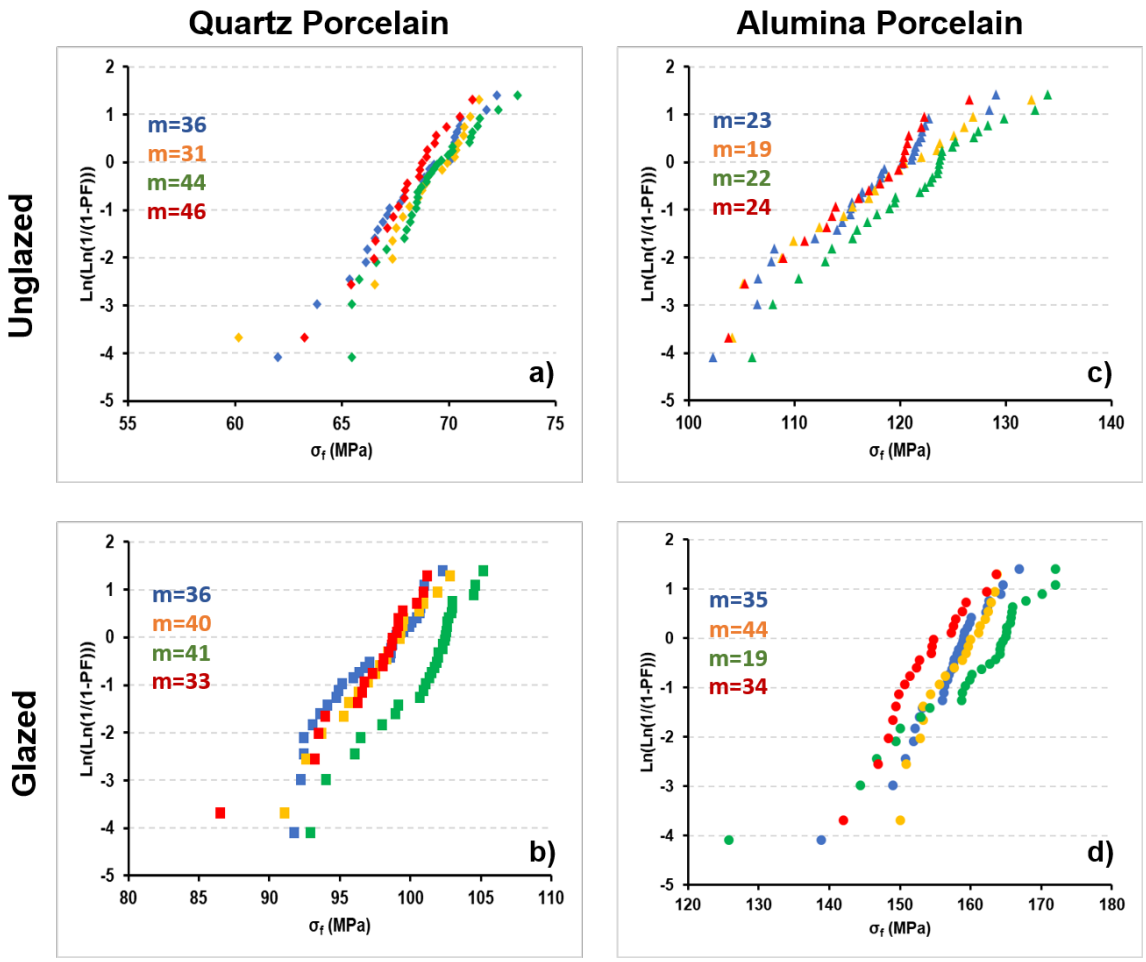

Figure 18. Stress at failure plotted against the Weibull distribution for the sample sets tested for the times noted: (a) unglazed quartz porcelain (b) glazed quartz porcelain (c) unglazed alumina porcelain and (d) glazed alumina porcelain.

It is evident from the four subplots that there are minimal changes in strength over the time interval evaluated. All the individual test groups show monomodal behavior indicating a single flaw population. Parametric evaluation (Figure 19), however, of the datasets presented in Figure 18, identifies a possible concurrent flaw population for the glazed alumina samples, constituting approximately 4% of the population, and a possible exclusive flaw population in the unglazed alumina porcelain sample set, constituting approximately 4% of the population.

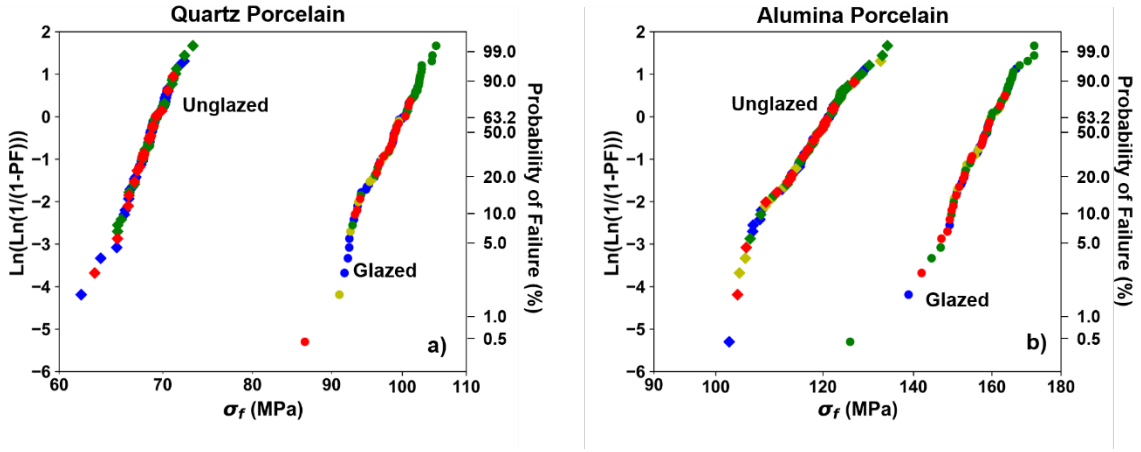

Figure 19. Parametric evaluation of atmospherically aged test specimen with blue, yellow, green and red markers representing samples tested after 0.01, 0.03, 0.1 and 0.3 years, respectively.

The unglazed and glazed alumina porcelains have a small exclusive and concurrent flaw population, respectively. The exclusive flaw population could arise from 1) changes in processing or 2) variation in mechanical testing. All samples were tested by the same operator removing issues related to testing and all samples were processed and fired together. There is no explanation for the exclusivity, but the contribution is small.

D. Origins of Failure

Fractography indicated failure initiated at the sample surface for unglazed porcelain, and at the body glaze interface or in the body for glazed porcelain. For specimen failing between the neutral axis and the specimen surface, several were found to be caused by inclusions and extrusion related defect (Fig. 20). Out of the four hundred test specimens, one failure was found to be caused by an extrusion defect and three from metal inclusions. However, no correlation was found between the origin of failure and exclusivity nor measured strength. Examples of failure origins are portrayed in Figure 21.

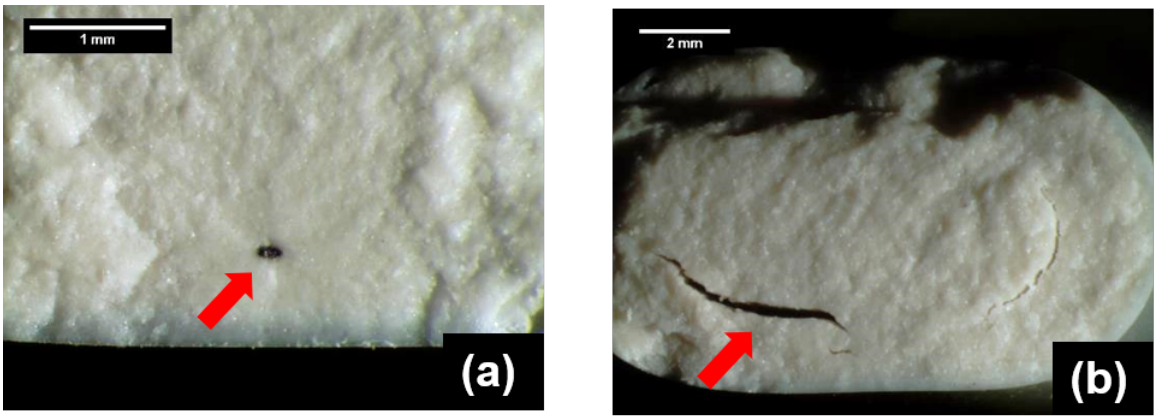

Figure 20. Failures due to (a) metal inclusions (3 total) and (b) an extrusion defect (1 total).

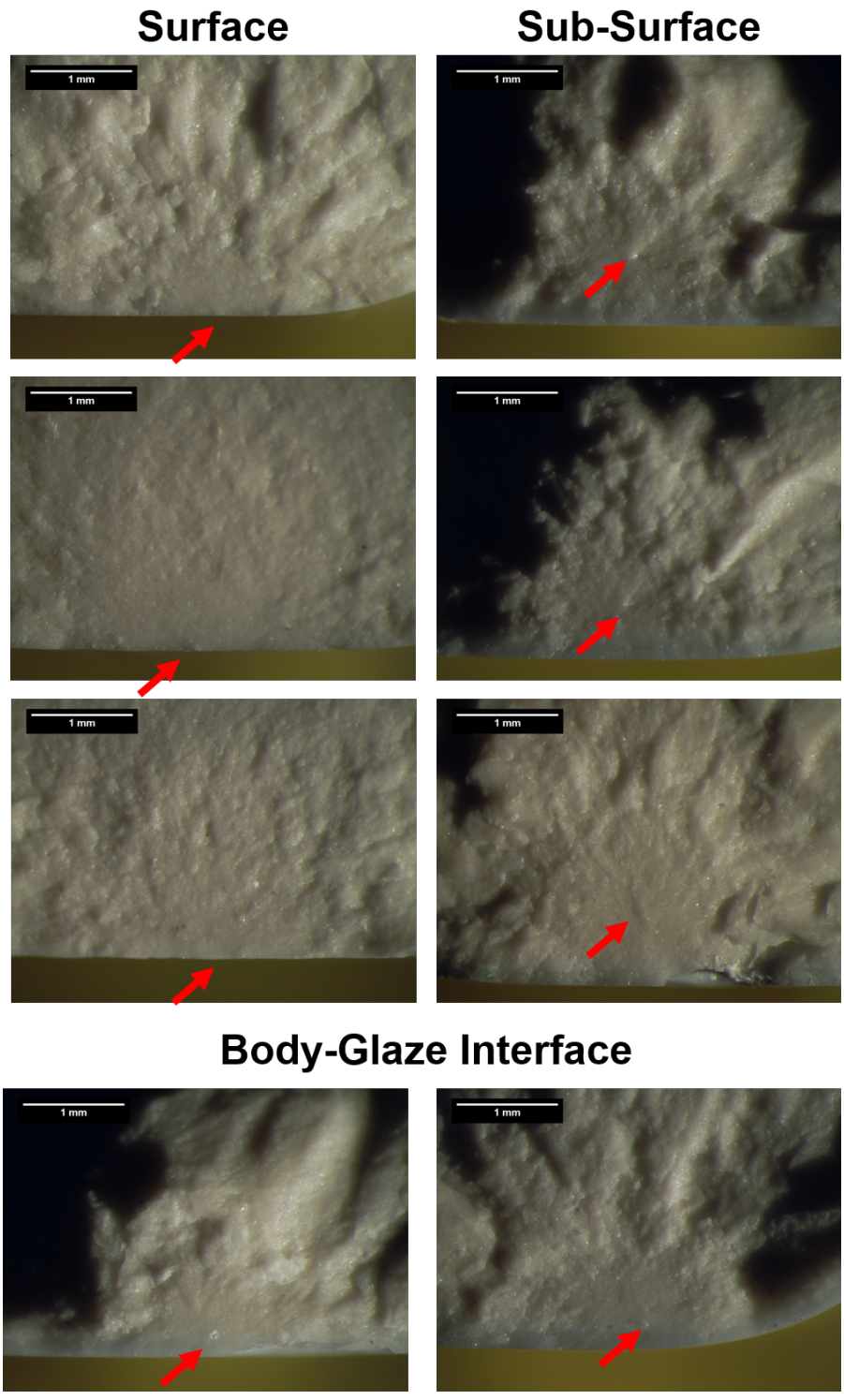

Figure 21. Examples of origins of failure. Surface failures occurred in unglazed samples whereas body failures occurred in glazed samples.

All unglazed test specimens were found to fail at the tensile surface of the test specimen. Further investigation via electron microscopy identified quartz grains to be the located at the fracture origin (Figure 23). Quartz grains at the failure origin are close in size to the calculated critical flaw sizes. Fracture markings shown in Figure 24 indicate failure initiates within the quartz particle rather than the surrounding matrix. Note that the fracture surface images are unetched and show no signs of radial cracking of the glass matrix: cracking only appears within the quartz grain.

Failure origins in glazed samples were also found to be quartz grains. However, multiple fracture origin locations were observed i.e. sub-surface and body-glaze interface due to the compressive stress generated at the glaze surface (Fig. 22).

It is not surprising that failure initiates in quartz grains. While porcelain cools during the heat treatment process, residual quartz grains contract significantly greater than the surround glass matrix due to the difference in CTE. This generates a radial tensile strain in the quartz grains (and tangential compression) which increases as a functions of grain size. Therefore, all quartz grains in the body have residual radial tensile strain. Strain is additive, and strain generated during mechanical testing then adds to the residual strain due to C.T.E. mismatch, resulting in a compounded strain in quartz grains during testing. When the strain limit, or critical strain, is reached in quartz grains, fracture initiates.[6]

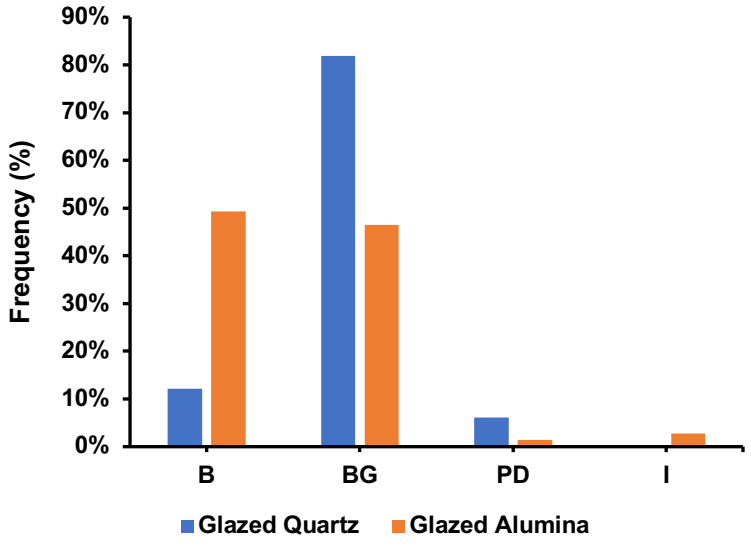

Figure 22. Frequency of fracture origin locations for quartz and alumina porcelain.

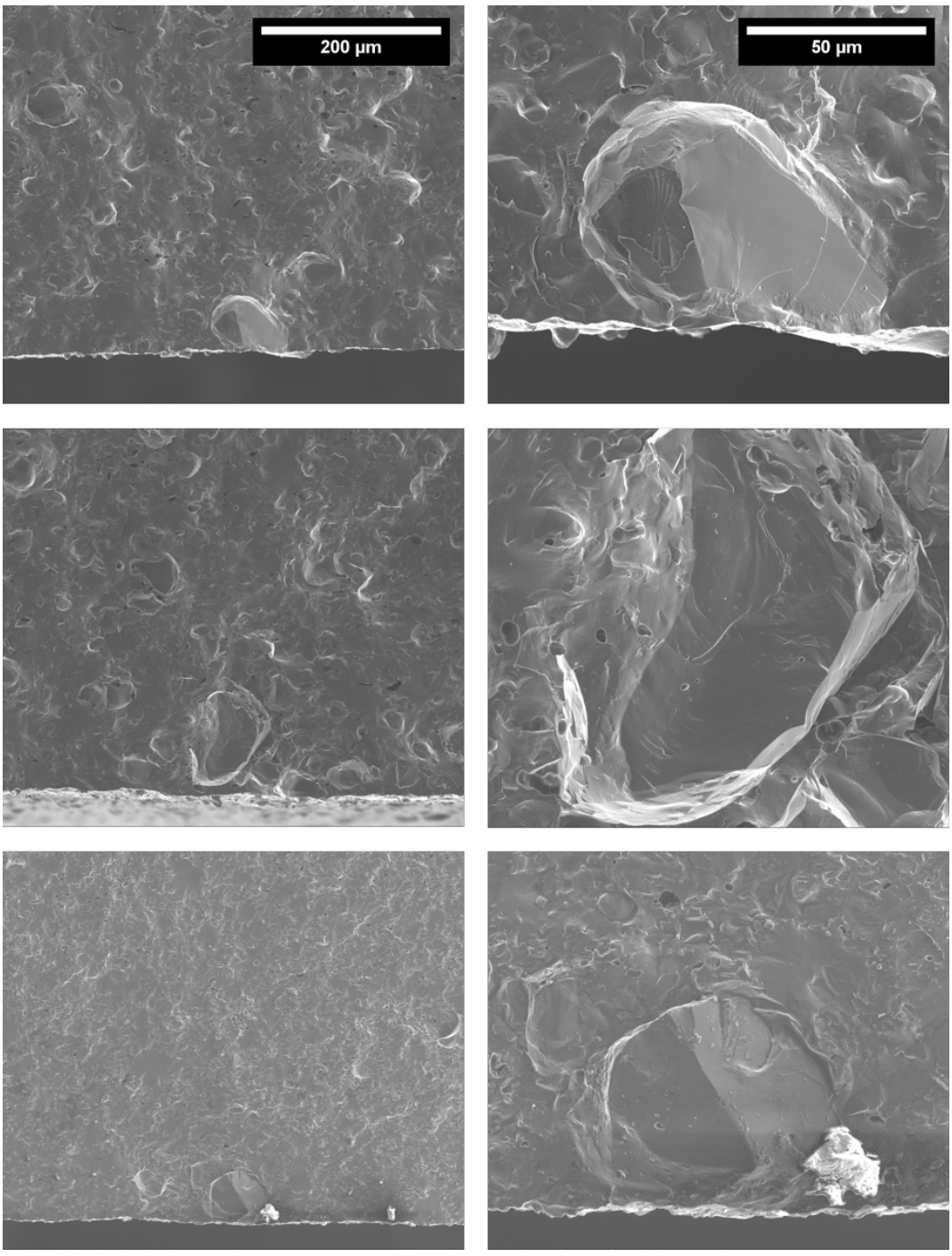

Figure 23. Quartz grain located at origin of failure (left column) and fracture markings on quartz grains indicating failure occurring within the quartz grain (right).

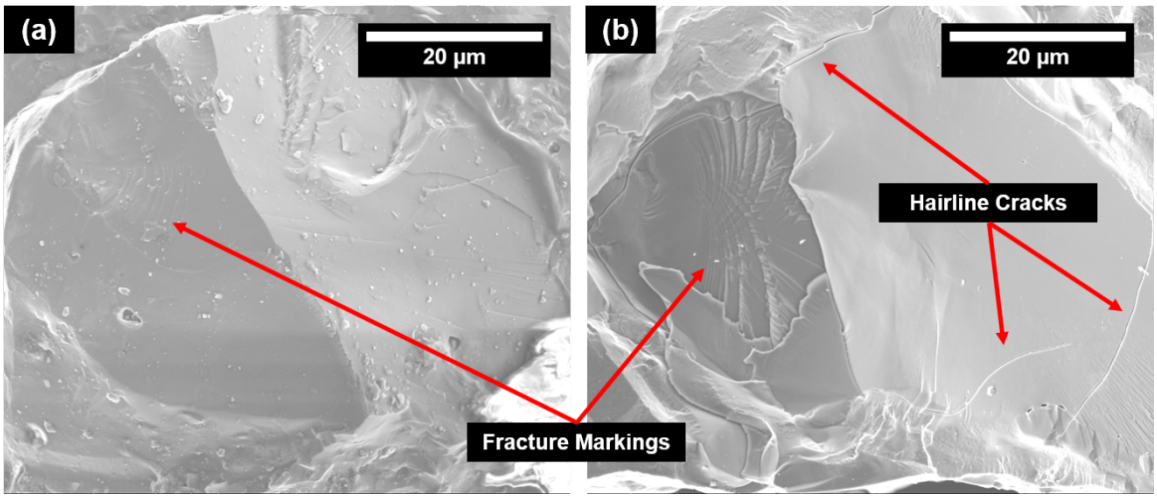

Figure 24. Fracture markings observed in quartz grains for (a) quartz porcelain and (b) alumina porcelain.

The initiation of failure within an individual quartz particle indicates two important conditions of quartz in porcelain: (1) the quartz particle is intimately bonded to the glass matrix (and failure does not initiate in the matrix nor the quartz-matrix interface); and (2) the elastic modulus of the quartz particle is higher than the surrounding matrix. The second condition could be modified to state that the failure strain for quartz is lower than the surrounding glass matrix due to the additive strain resulting from CTE mismatch during cooling. This strain can be further exaggerated by difference in CTE along various crystallographic planes. Therefore, the act of mechanically testing adds additional strain to a quartz grain resulting in cracking of the quartz grain. To postulate that the elastic modulus for quartz is greater than the surrounding matrix is not unreasonable as quartz is highly anisotropic. Pinto (and others) documented the elastic modulus anisotropy in quartz with greater than one order of magnitude difference (6.9 to 105.9 GPa) in stiffness constant between crystallographic directions.[6] Therefore, it is plausible that failure will occur when the applied stress is perpendicular to the stiffest crystallographic direction.

Failure can be expected to occur in the largest quartz grain in the applied stress field. As grain size (critical flaw size) increases, the stress intensity factor (K_I) increases per Griffith's theory:

$$K_I = \sigma Y \sqrt{c} \tag{14}$$

Where σ is the applied stress, Y is the shape factor and c is the flaw or, in the case of quartz porcelain, quartz grain size. In a quartz porcelain it is fair to assume the shape factor is equivalent for all grain since the geometries similar. Figure 25 shows two quartz grain (θ_1 and θ_2) intimately bonded to a glass matrix which is being subjected to an applied tensile stress. In this situation, both grains see equivalent strain (stress) since the elastic modulus is of the glass phase is constant and have identical fracture toughness (K_{IC}) since this is a material property. Despite grain 1 and grain 2 exhibiting equivalent strain, grain 1 will be subjected to a higher stress intensity because of the relationship with respect to flaw size. Therefore, fracture will initiate once a sufficient strain (stress) is applied to cause K_I to equal K_{IC}. This will occur in the larger grain which is subjected to a higher initial stress intensity.

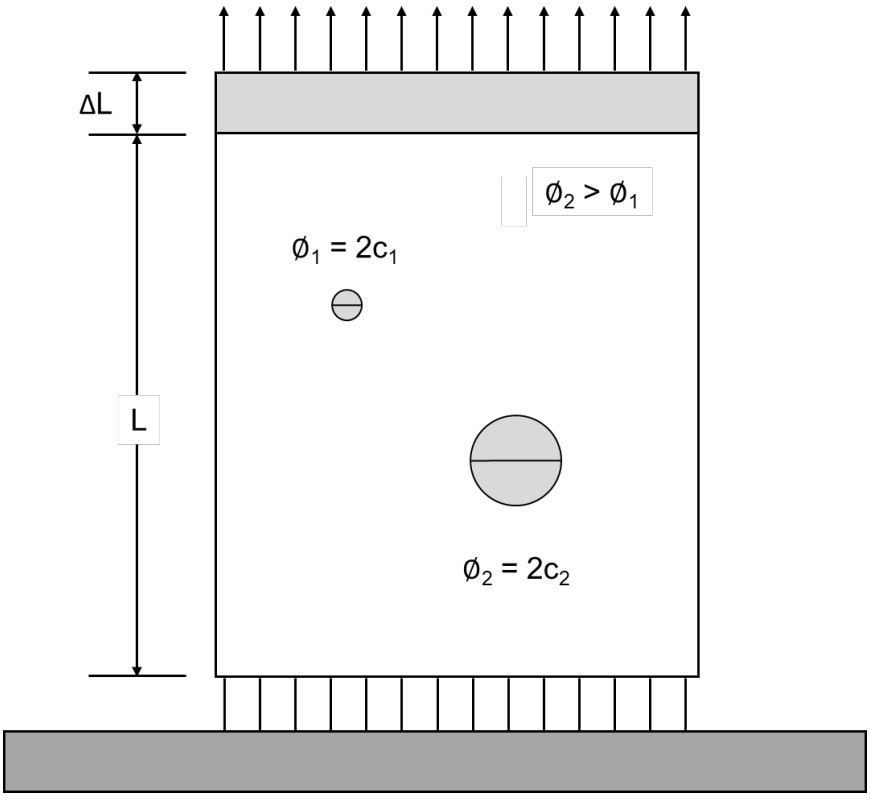

Figure 25. Schematic showing effect of grain size on strength in a stress field.

The parametric evaluation, in addition to showing monomodal behavior, also shows that the strength data for each decade, or duration of aging, are well dispersed across the Weibull distributions. This indicates that all specimens in each test group belong to the same dataset. Therefore, the minimum, maximum and characteristic strengths along with Weibull moduli can be reported based on 100 data points for each test group (Table. XIII).

Table XIII. Minimum, maximum, and characteristic strengths of quartz and alumina porcelain based on 100 data points along with Weibull moduli.

Test Group	$\sigma_{f,\,min.}$ (MPa)	$\sigma_{f,\,Char}$ (MPa)	$\sigma_{f,\,max.}$ (MPa)	Weibull Modulus
Quartz Porcelain	60.2	69.3	73.2	40
Glazed Quartz Porcelain	86.5	100.4	105.2	35
Alumina Porcelain	102.3	121.3	133.9	22
Glazed Alumina Porcelain	125.7	159.8	171.9	27

Figure 26 and 27 shows the calculated critical flaw sizes and strain at failures for the unglazed porcelains plotted against a Weibull distribution. Calculated critical flaw sizes were determined to be between 40 and 80 μm for both porcelains with equivalent ranges of strain required to cause catastrophic failure. Table XIV shows the calculated maximum and minimum flaw sizes. This indicates both porcelains have similar strength limiting flaws. This observation is not surprising as both bodies were processed with the same industrial process at the same time (i.e., equivalent manufacturing environments result in equivalent flaw populations). Differences in the porcelain composition have no correlation with the flaw population and scale with the elastic modulus of the porcelain body. This indicates that flaw populations introduced in the processing of the test specimen are smaller than the effective size of the strained quartz grains. Flaw size and strain at failure are not shown for the glazed samples due to the unknown effects of the glaze on the elastic modulus.

Table XIV. Minimum and maximum calculated critical flaw sizes

Critical Flaw Size (μm)		
	Quartz Porcelain	Alumina Porcelain
Min.	40	37
Max.	59	63

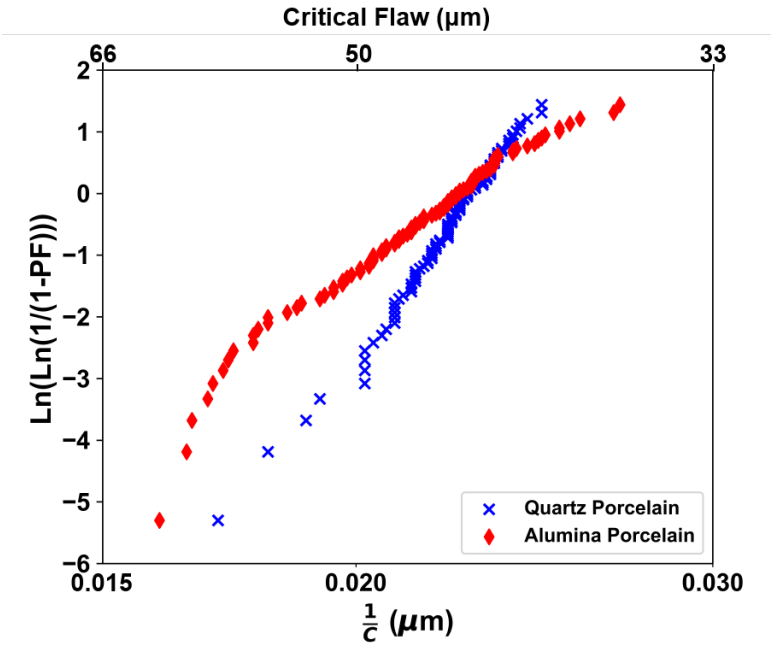

Figure 26. A Weibull distribution plotted as a function of the inverse critical flaw size (1/c) for unglazed quartz and alumina porcelains.

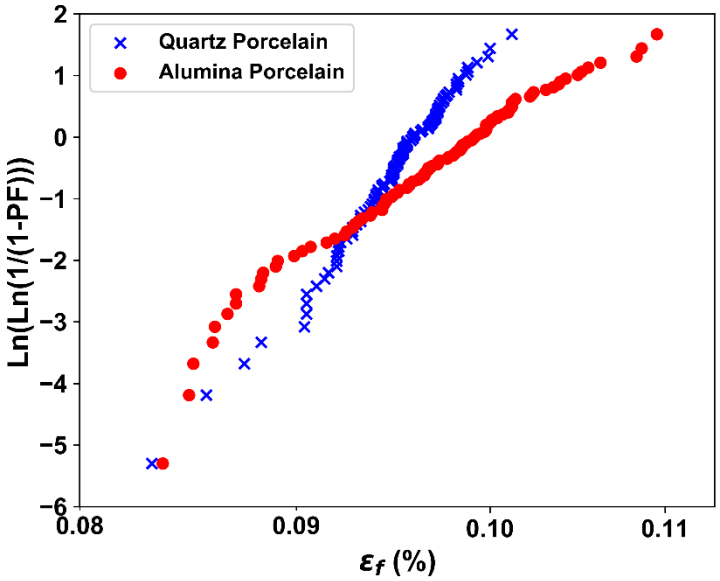

Figure 27. Strain at failure plotted against a Weibull distribution for unglazed quartz and alumina porcelain.

In conclusion, under identical processing conditions, the porcelain compositions have similar critical flaw size populations. Therefore, the elastic modulus of the porcelain is directly controlling the strength, not residual quartz grain size. Since quartz grains are witnessed as the origin of failure, it can be concluded that inherent process defects in the tested porcelain are smaller than residual quartz grains. The elastic modulus has been shown to be affected by firing temperature which determines the density (degree of porosity) and by the composition of the porcelain body.[33-35] Therefore, these two variables can be used to develop a high strength porcelain body. The CTE of the glass phase could be increased to match that of quartz, however, it has been shown to be impossible in an alumina-saturated glass composistion.[36]

E. Aging in the Presence of Steam

Screening studies at 550 kPa and 1900 kPa (80 psi and 275 psi, respectively), were used to assess the effects of high-pressure steam on the strength of porcelain. Unglazed and glazed alumina porcelain samples were tested after being subjected to 1, 3, 6, 12 and 30 autoclaving cycles. Results are shown in Table XV illustrate an increase in strength for the unglazed samples but no change in the strength of glazed porcelain samples. A sample set of 30 bend bars were then cycled 30 times to confirm preliminary results.

Table XV. Results of autoclave screening study (5 test specimen per test).

Cycles	0	1	3	6	12	30
Alumina Porcelain – 80 psi (MPa)	117.1 ±6.3	125.0 ±2.9	126.6 ±8.4	121.6 ±8.4	127.0 ±5.8	N/A
Glazed Alumina Porcelain – 80 psi (MPa)	157.2 ±5.4	158.1 ±7.5	170.1 ±3.8	163.5 ±10.0	163.0 ±5.8	N/A
Alumina Porcelain – 275 psi (MPa)	117.1 ±6.3	130.6 ±5.8	130.6 ±4.2	130.5 ±7.6	139.0 ±6.7	142.6 ±15.0
Glazed Alumina Porcelain – 275 psi (MPa)	157.2 ±5.4	166.5 ±2.2	166.9 ±7.6	157.6 ±4.8	166.1 ±3.8	162.9 ±4.3

Weibull plots showing flexural strengths of a statistically relevant sample set post-aging in the presence of steam compared to benchmark samples are shown in Figure 28. It is evident that there is a significant increase in strength for unglazed porcelain. Glazed test specimens show no change in strength. Small changes in Weibull moduli are seen for

unglazed test specimen, however, reported values are higher than those typically reported in the literature for brittle materials.[37-39]

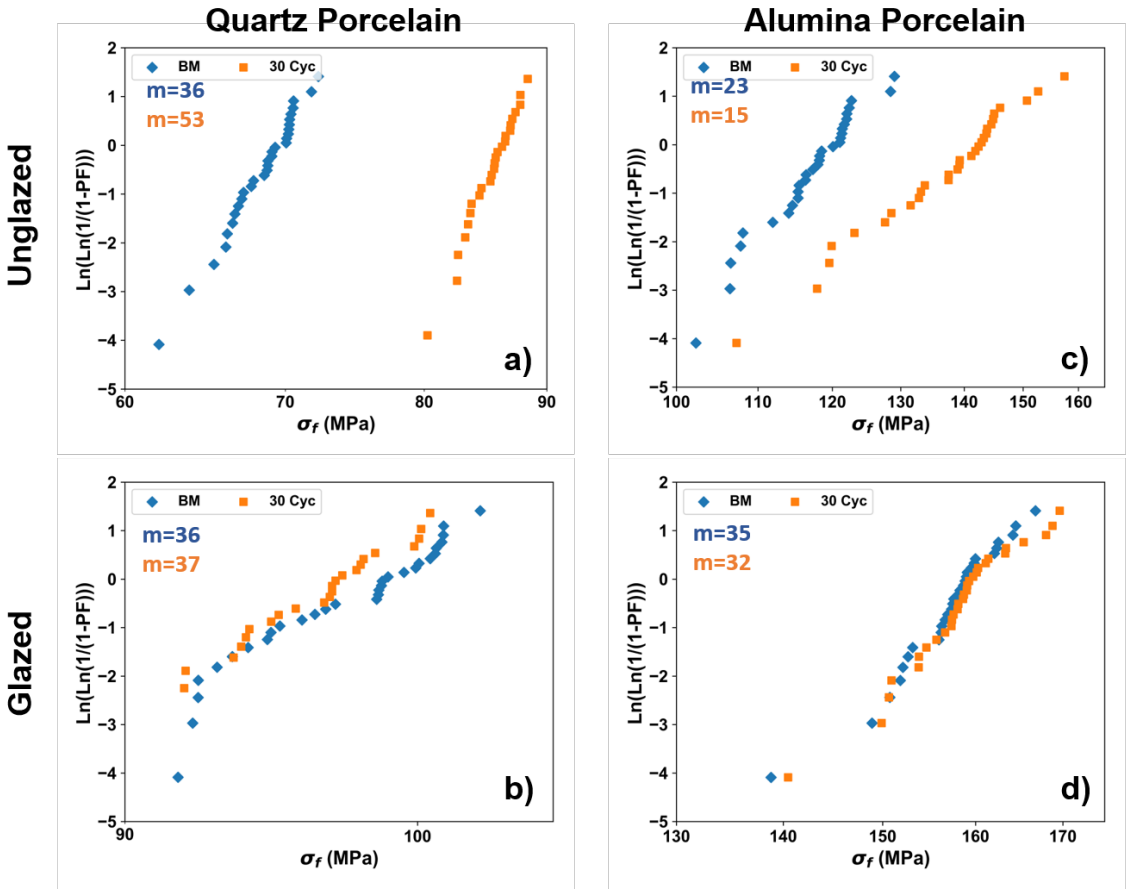

Figure 28. Weibull plots comparing strengths post-exposure to high pressure steam to bench mark samples for (a) quartz porcelain, (b) glazed quartz porcelains, (c) alumina porcelain, and (d) glazed alumina porcelain.

To investigate the increase in strength of the porcelains post autoclaving, scanning electron images were collected of the test specimen surfaces. From Figure 29, it is evident that the high-pressure steam is altering the surface. However, the strengthening mechanism remains unclear.

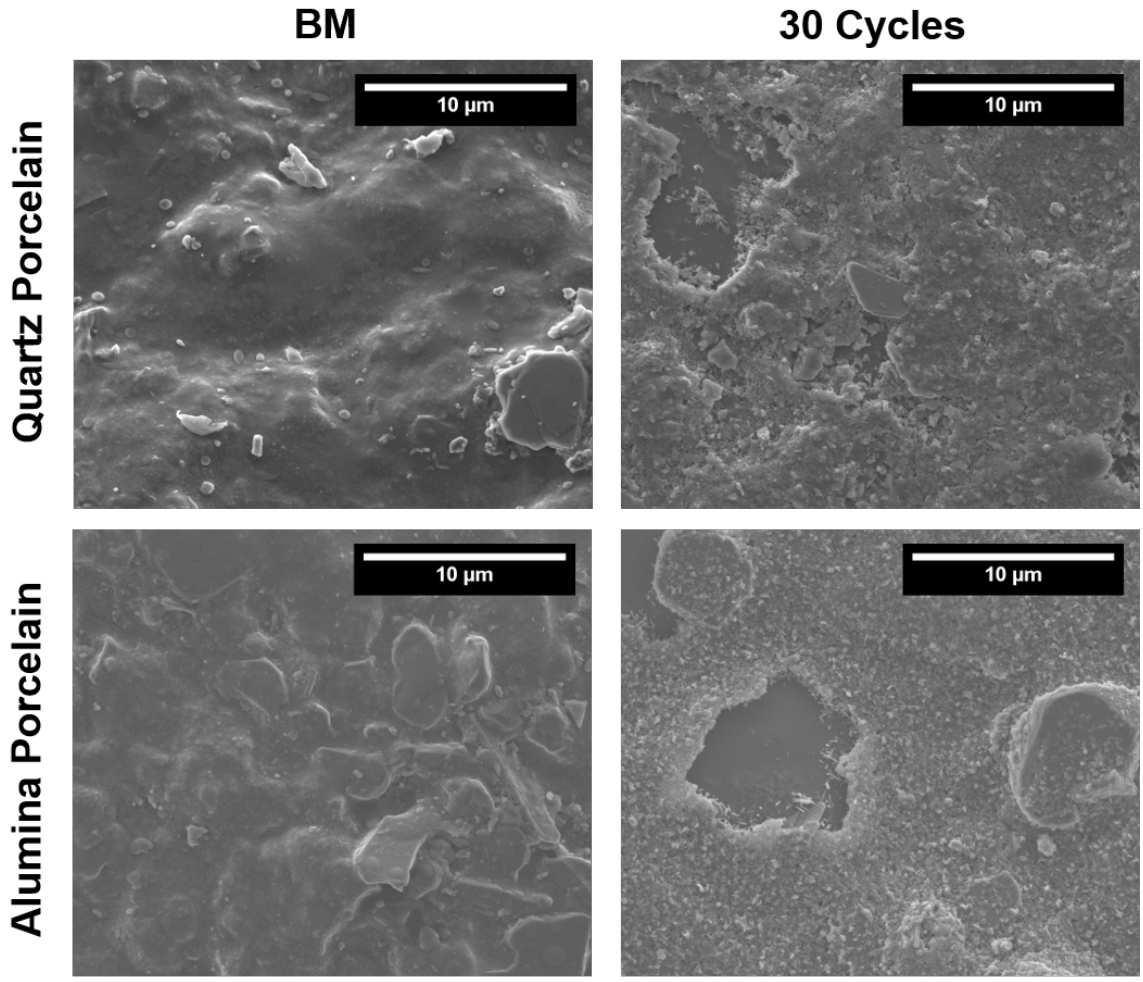

Figure 29. Surfaces of quartz and alumina porcelain before and after exposer to high-pressure steam.

F. Matrix Cracking

Several researchers have claimed that quartz inversion at 573°C leads to microcracking of the amorphous maxtrix.[9-14,40] Cracking of the matrix in the vicinity of quartz particles is proposed to be responsible for degradation of strength over time. Note however that the fractography results do not show any evidence of matrix cracking. To facilitate the evaluation of the microstructure, chemical etching has been typically invoked. Even the polishing of the porcelain microstructure, however, can lead to damage of the glass matrix in the vicinity of quartz particles.

Crack growth is encouraged by (1) temperature fluctuations generating localized stresses at the crack tip due to thermal expansion and (2) chemical attack at the crack tip.[41]

Microcracks would be expected to elongate from cyclic exposure to high pressure steam from both these variables resulting in a weaker test specimen. Strengths, however, were not found to deteriorate.

Etched fracture surfaces are typically used to show the presence of microcracks (Fig. 1). It was found that tensile regions undergo preferential degradation when exposed to a chemical etch such as hydrofluoric acid. Figure 30 shows a scanning electron photomicrograph of a polished porcelain body-glaze interaction region for the alumina porcelain in this study. This specimen was subjected to a light etch (5 wt% HF, 0 °C, 10 sec). Glazes are formulated to create a compressive surface which increase the component strength. A glaze in compression results in tension in the underlying porcelain body. It is evident that the tensile region below the glaze exhibits preferential etching. However, the glaze, in compression, and the bulk body, in a neural state, do not appear to have been altered.

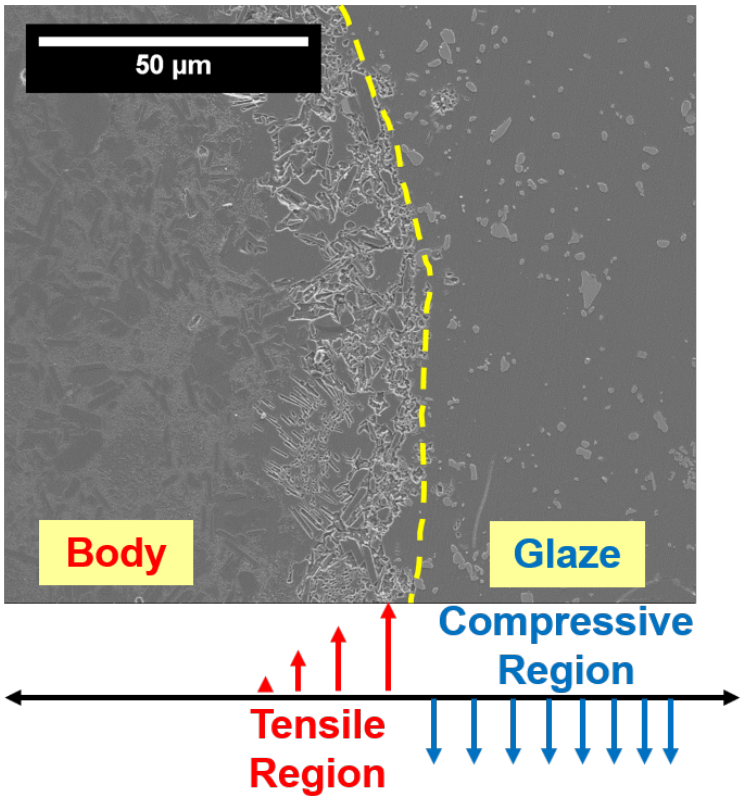

Figure 30. Polished section showing the body-glaze interface region for the alumina porcelain after a light hydrofluoric acid etch.

It is reasonable to extrapolate this result to the similar stress states present around quartz particles in the amorphous matrix due to the thermal expansion mismatch between quartz and the glass matrix. During cooling, quartz contracts more than the matrix causing radial tension and tangential compression to develop in the glass matrix (and the quartz particles).[42] Due to tension in the glass matrix, chemical etching will preferentially attack the glass matrix surrounding the quartz grains. Figure 31(a) shows a microstructure after exposure to light etching conditions. Hairline cracks develop in the matrix around the quartz grain. The cracks are due to radial tension developed due to CTE mismatch during cooling. When a more aggressive etch is used (Fig. 31(b)) large craters form around the quartz grain in the glass matrix.

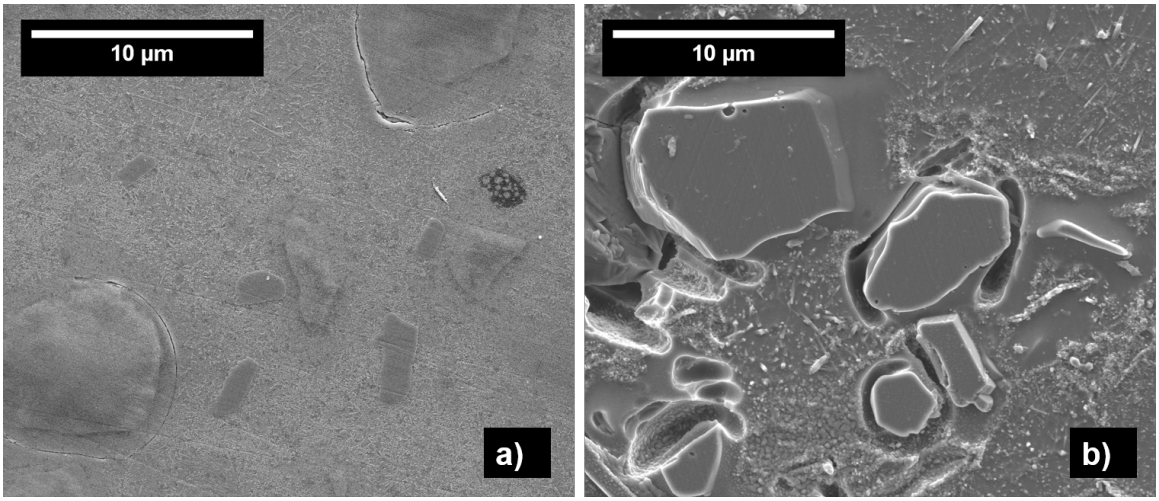

Figure 31. Porcelain microstructures after etched (a) for 10 seconds in 5 wt% HF at 0 °C and (b) 20 seconds in 20 wt% HF at room temperature

G. Role of Etching on Strength

To explore the effects of cracks generated by chemical attack, a screening study was conducted utilizing 5 samples per test condition. Test specimen were submerged in 5,

10, and 20 wt% HF for 10 seconds at room temperature then neutralized with a calcium carbonate suspension. After rinsing and ultrasonicating the test specimen with deionized water, specimens were tested in flexure. The results shown in Fig. 32 shows statistically identical datasets indicating that the formation of microcracks surrounding quartz grains have no effect on strength. Therefore, it can be concluded that failure initiates in the quartz grain. Strength is dependent on the overall elastic modulus of the porcelain system which dictates when sufficient strain is applied to cause the quartz grain, already in a stressed state from cooling, to fracture as addressed previously.

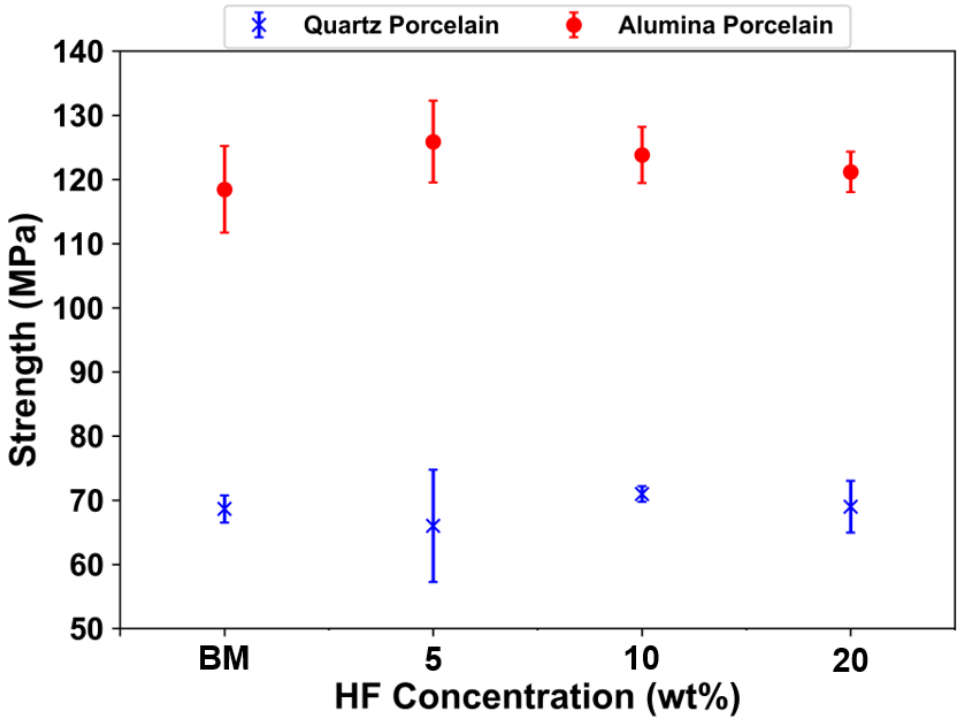

Figure 32. Strength of porcelain test specimen after exposure to 5, 10 and 20 wt% HF. Unetched benchmark samples are represented as "BM".

IV. SUMMARY AND CONCLUSIONS

Strength data obtained through 4-point flexural testing of quartz and alumina porcelain indicates linear elastic failure behavior. Both porcelain compositions had similar critical flaw sizes and exhibited similar failure strains. Unglazed porcelains consistently failed at the tensile surface; however, glazing caused failure origins to be pushed towards the neutral axis. Strength limiting flaw populations for both porcelains were determined to be large quartz grains. This indicates that the additive strain resulting from CTE mismatch in the quartz grain are larger than process-generated defects.

Age effects on strength were not observed after 0.3 years of real time aging in a natural environment allowing datasets to be combined resulting in characteristic strengths and Weibull moduli to be reported based on 100 data points. Cyclic exposure to high-pressure steam resulted in a significant increase in strength of unglazed, but no effect on glazed porcelain rods. Microcracks were not identified in any samples suggesting sample strengths will not degrade with continued aging. All results were obtained using a novel test specimen geometry which allowed for defect-free extrudates.

Fractographic analysis has found that failure initiates in quartz grains. This finding differs from previous theories which suggest failure initiates in the matrix from cracking resulting from CTE mismatch. It is proposed that these theories were established from over etch micrographs. Etching has been found to preferentially remove stressed regions of the glass phase.

V. FUTURE WORK

Strengths of the four test groups will continue to be monitored for the next three decades allowing conclusions to be made on a fully characterize porcelain body. 30 samples per test group per decade will be tested. For equivalent comparison of unglazed samples, the surface exposed to the atmosphere during firing will be loaded in tension. Dates of testing are shown in Table XVI. Figure 32 shows test specimen aging on the roof of the McMahon Building at Alfred University.

Table XVI. Test schedule for porcelain samples.

Years	Days	Date
1	365	4/10/2019
3	1095	4/9/2021
10	3650	4/7/2028
30	10950	4/2/2048

Figure 33. Test specimen aging on the roof of the McMahon Engineering Building at Alfred University during an unusually sunny day.

VI. REFERENCES

1. W. M. Carty and U. Senapati, "Porcelain-Raw Materials, Processing, Phase Evolution, and Mechanical Behavior," *Journal of the American Ceramic Society,* **81** [1] 3-20 (1998).

2. A. Zoellner, "Zur Frage Der Chemischen Und Physikalischen Natur Des Porzellans," *Sprechsaal,* **41** [35] 471-3 (1908).

3. L. Mattyasovszky-Zsolnay, "Mechanical Strength of Porcelain," *Journal of the American Ceramic Society,* **40** [9] 299-306 (1957).

4. G. I. Gilchrest and T. A. Klinefelter, "Experimental Investigation of Porcelain Mixes," *Electric Journal,* **15** 79 (1918).

5. S. Warshaw and R. Seider, "Comparison of Strength of Triaxial Porcelains Containing Alumina and Silica," *Journal of the American Ceramic Society,* **50** [7] 337-42 (1967).

6. B. M. Pinto, "Effect of Filler Particle Size on Porcelain Strength "; M.S. Thesis. Alfred University, 2001.

7. S. Maity and B. Sakar, "Development of High-Strength Whiteware Bodies," *Journal of the European Ceramic Society,* **16** 1083-8 (1996).

8. W. Blodgett, "High-Strength Alumina Porcelains," *American Ceramic Society Bulletin,* **40** [2] 74-7 (1961).

9. J. Liebermann, "Special Benefits of Bauxite for a Stable Porcelain Microstructure in High-Voltage Insulation," *American Ceramic Society Bulletin,* **96** [7] 32-5 (2017).

10. J. Liebermann, "Avoiding Quartz in Alumina Porcelain for High-Voltage Insulators," *American Ceramic Society Bulletin,* **80** [6] 37-42 (2001).

11. J. Liebermann, "Microstructure Properties and Product Quality of Strength-Stressed High-Voltage Insulators," *American Ceramic Society Bulletin,* **82** [2] 39-46 (2003).

12. P. Ranachowki, F. Rejmund, Z. Ranachowski, A. Pawelek, and A. Platkowski, "Aluminous Porcelain Degradation Study Using Mechanoacoustic and Microscopic Methods," *Archives of Electrical Engineering,* **60** [2] 109-28 (2011).

13. P. Ramaswamy, S. Vynatheya, and S. Seetharamu, "Significance of Structure – Property Relationship in Alumina Based Porcelain Insulators to Achieve Quality," *Bulletin of Materials Science,* **28** [7] 681-8 (2005).

14. Y. Ohya, Y. Takahashi, M. Murata, and Z. Nakagawa, "Acoustic Emission from a Porcelain Body During Cooling," *Journal of the American Ceramic Society,* **48** 445-8 (1999).

15. G. Stathis, A. Ekonomakou, C. J. Stournaras, and C. Ftikos, "Effect of Firing Conditions , Filler Grain Size and Quartz Content on Bending Strength and Physical Properties of Sanitaryware Porcelain," *Journal of the European Ceramic Society,* **24** 2357-66 (2004).

16. M. Jackson and B. Mills, "Dissolution of Quartz in Vitrified Ceramic Materials," *Journal of Materials Science,* **32** 5295-304 (1997).

17. Y. Iqbal and W. E. Lee, "Fired Porcelain Microstructures Revisited," *Journal of the American Ceramic Society,* **82** [12] 3584-90 (1999).

18. Y. Iqbal and W. E. Lee, "Microstructural Evolution in Triaxial Porcelain," *Journal of the American Ceramic Society,* **83** [12] 21-7 (2000).

19. G. D. Quinn, *Fractography of Ceramics and Glasses;* pp. 5-1. 2007.

20. M. R. Mitchell, R. E. Link, G. D. Quinn, B. T. Sparenberg, P. Koshy, and L. K. Ives, "Flexural Strength of Ceramic and Glass Rods," *Journal of Testing and Evaluation,* **37** [3] 1-23 (2009).

21. S. Rodrigues, J. Ferracane, and A. Bona, "Flexural Strength and Weibull Analysis of a Microhybrid and a Nanofill Composite Evaluated by 3- and 4-Point Bend Tests," *Dental Materials,* **24** [3] 426-31 (2008).

22. A. C1161-02, "Standard Test Method for Flexural Strength of Advanced Ceramics at Ambient," *ASTM International,* **West Conshohocken, PA** (2002).

23. M. Modugno, A. Wereszczak, and S. Waters, "Toward Interpreting Failure in Sintered-Silver Interconnection Systems," *Additional Conferences (Device Packaging, HiTEC, HiTEN, & CICMT),* **2016** [HiTEC] 234-41 (2016).

24. A. C1239-00, "Standard Practice for Reporting Uniaxial Strength Data and Estimating Weibull Distribution Parameters for Advanced Ceramics," *ASTM International,* **West Conshohocken, PA** (2000).

25. S. Sane and R. Cook, "Effect of Grinding and Firing Treatment on the Crystalline and Glass Content and the Physical Properties of Whiteware Bodies," *Journal of the American Ceramic Society,* **34** [5] 145-69 (1951).

26. W. Lerdprom, "Firing of Porcelain"; Alfred University, 2014.

27. A. C737-14, "Standard Test Method for Water Absorption, Bulk Density, Apparent Porosity, and Apparent Specific Gravity of Fired Whiteware Products, Ceramic Tiles, and Glass Tiles," *ASTM International,* **West Conshohocken, PA** (2014).

28. A. Bedford, W. Fowler, and K. Liechti, *Statics and Mechanics of Materials*. Appendix A, 2003.

29. A. A. Griffith, "The Phenomena of Rupture and Flow in Solids," *Philosophical Transactions of the Royal Society,* **221** 163-98 (1921).

30. W. M. Carty, K. Sieg, B. M. Pinto, and M. Kumar, "A New Technique for Measuring the Fracture Surface Energy of Ceramics"; pp. 243-50 in *Fractography of Glasses and Ceramics V: Ceramic Transactions.*

31. D. Levine, P. Ramsey, and R. Smidt, *Applied Statistics for Engineers and Scientists;* p. 671. 180-220, 2001.

32. T. Thadewald and H. Buning, "Jaque-Bera Test and Its Competitors for Testing Normality-a Poer Comparison," *Journal of Applied Statistics,* **34** [1] 18 (2007).

33. C. Magee, "Strength Development of Porcelain Bodie During Firing"; B.S. Thesis. Alfred University, 2012.

34. A. Fredell, "Microstructure Evolution and Fractography of Sintered Alumina"; B.S. Thesis. Alfred University, 2013.

35. C. Hoag, "Strength Evolution in Alumina During Sintering and Densification"; B.S Thesis. Alfred University, 2013.

36. E. Skovira, "Properties of the Porcelain Glass Phase"; M.S. Thesis. Alfred University, 2006.

37. L. Gorjan and M. Ambrozic, "Bend Strength of Alumina Ceramics: A Comparison of Weibull Statisitcs Based on Very Large Experimental Data Set," *Journal of the European Ceramic Society,* **32** 1221-7 (2012).

38. C. Klein, "Characteristic Strength, Weibull Modulus, and Failure Probability of Fused Silica Glass," *Optical Engineering,* **48** [11] 1-10 (2009).

39. M. Madjoubi, C. Bousbaa, M. Hamidouche, and N. Bouaouadja, "Weibull Statistical Analysis of the Mechanical Strength of a Glass Eroded by Sand Blasting," *Journal of the European Ceramic Society,* **19** 2957-62 (1999).

40. T. Soma, M. Matsui, and N. Yamamoto, "Applicability of Crack Propagation Data to Failure Prediction in Porcelain," *Journal of the American Ceramic Society,* **63** 166-9 (1980).

41. S. Wiederhorn, T. Fett, G. Rizzi, M. Hoffmann, and J.-P. Guin, "The Effect of Water Penetration on Crack Growth in Silica Glass," *Engineering Fracture Mechanics,* **100** 3-16 (2013).

42. R. W. Davidge, "Mechanical Behaviour of Ceramics," 87 (1980).

VII. APPENDIX

Table XVII. 0.01 year strength data.

	Quartz Porcelain		Alumina Porcelain		Glazed Quartz Porcelain		Glazed Alumina Porcelain	
ID#	Thickness (mm)	Force (N)	Thickness (mm)	Force (N)	Thickness (mm)	Force (N)	Thickness (mm)	Force (N)
1	7.30	638.68	7.18	1189.47	7.75	1215.72	7.61	1839.39
2	7.27	677.14	7.18	1044.52	7.72	1229.87	7.64	1780.53
3	7.29	723.53	7.20	1196.66	7.72	1246.32	7.59	1832.77
4	7.29	718.89	7.22	1169.21	7.72	1178.89	7.62	1862.86
5	7.30	673.44	7.21	1202.64	7.74	1233.60	7.62	1864.00
6	7.31	684.90	7.18	1259.27	7.73	1138.11	7.64	1939.29
7	7.28	706.10	7.19	1127.46	7.76	1249.20	7.67	1659.05
8	7.26	713.26	7.21	1211.16	7.73	1223.91	7.63	1882.14
9	7.29	721.00	7.20	1140.89	7.69	1186.76	7.62	1794.74
10	7.29	684.25	7.19	1166.56	7.74	1126.56	7.63	1796.02
11	7.28	718.25	7.19	1204.68	7.72	1155.87	7.61	1828.42
12	7.31	712.10	7.19	1061.22	7.73	1234.02	7.62	1843.88
13	7.26	695.09	7.20	1139.54	7.74	1134.72	7.62	1899.58
14	7.25	729.26	7.21	1211.48	7.75	1215.49	7.59	1761.66
15	7.26	727.43	7.27	1083.50	7.74	1155.33	7.67	1867.55
16	7.26	681.46	7.25	1228.13	7.72	1203.05	7.63	1837.70
17	7.29	654.88	7.14	1121.87	7.72	1154.40	7.64	1853.38
18	7.31	692.15	7.21	1280.89	7.71	1200.93	7.61	1772.54
19	7.29	706.34	7.22	1223.13	7.74	1222.02	7.65	1881.27
20	7.34	734.06	7.14	1111.30	7.72	1226.31	7.66	1902.64
21	7.27	705.40	7.19	1195.14	7.74	1236.30	7.59	1847.30
22	7.30	708.67	7.15	1144.48	7.74	1177.95	7.62	1852.11
23	7.26	670.03	7.17	1172.20	7.77	1206.16	7.59	1823.67
24	7.29	695.19	7.24	1187.85	7.75	1136.92	7.61	1820.53
25	7.27	717.93	7.22	1115.71	7.73	1222.46	7.62	1861.30
26	7.26	711.73	7.19	1122.51	7.76	1143.60	7.59	1905.19
27	7.29	688.83	7.21	1171.22	7.73	1144.33	7.58	1717.49
28	7.27	691.00	7.17	1055.15	7.72	1159.58	7.59	1931.45
29	7.26	700.41	7.19	1007.08	7.76	1192.64	7.60	1887.57
30	7.29	720.26	7.23	1164.02	7.77	1226.30	7.55	1852.73

Table XVIII. 0.03 year strength data.

	Quartz Porcelain		Alumina Porcelain		Glazed Quartz Porcelain		Glazed Alumina Porcelain	
ID#	Thickness (mm)	Force (N)	Thickness (mm)	Force (N)	Thickness (mm)	Force (N)	Thickness (mm)	Force (N)
1	7.30	728.14	7.25	1245.89	7.75	1122.46	7.61	1895.35
2	7.29	617.31	7.24	1104.86	7.75	1212.69	7.62	1847.12
3	7.30	735.71	7.18	1152.58	7.70	1232.24	7.62	1860.48
4	7.30	695.72	7.23	1089.04	7.72	1209.74	7.64	1781.29
5	7.31	711.26	7.19	1035.16	7.77	1196.13	7.59	1876.78
6	7.31	705.14	7.19	1180.43	7.74	1197.58	7.63	1802.73
7	7.30	717.89	7.19	1162.09	7.73	1217.20	7.60	1875.04
8	7.31	713.23	7.21	1210.95	7.72	1165.26	7.62	1914.69
9	7.31	701.93	7.24	1210.32	7.73	1234.12	7.65	1816.52
10	7.31	726.88	7.23	1189.41	7.71	1247.41	7.63	1829.41
11	7.32	691.02	7.22	1166.30	7.71	1207.28	7.62	1887.69
12	7.32	726.43	7.24	1275.67	7.72	1226.02	7.62	1873.86
13	7.32	734.61	7.23	1147.53	7.71	1136.91	7.66	1896.37
14	7.32	730.63	7.22	1233.60	7.76	1145.79	7.61	1824.88
15	7.31	697.06	7.23	1156.40	7.70	1188.29	7.63	1764.44
16	7.30	706.70	7.26	1138.68	7.71	1177.13	7.63	1877.25
17	7.29	708.36	7.19	1024.85	7.73	1206.98	7.64	1923.58
18	7.32	699.87	7.21	1251.52	7.73	1165.38	7.61	1910.49
19	7.28	725.65	7.21	1314.15	7.72	1209.29	7.69	1840.78
20	7.28	719.84	7.20	1236.62	7.72	1191.71	7.61	1801.19

Table XIX. 0.1 year strength data.

	Quartz Porcelain		Alumina Porcelain		Glazed Quartz Porcelain		Glazed Alumina Porcelain	
ID#	Thickness (mm)	Force (N)	Thickness (mm)	Force (N)	Thickness (mm)	Force (N)	Thickness (mm)	Force (N)
1	7.28	700.49	7.20	1312.53	7.71	1236.05	7.63	1952.11
2	7.27	708.80	7.22	1165.42	7.75	1256.88	7.60	1461.18
3	7.29	688.45	7.20	1214.05	7.76	1248.64	7.60	1918.92
4	7.29	712.58	7.21	1227.93	7.75	1188.85	7.61	1885.17
5	7.29	728.70	7.22	1294.25	7.75	1264.03	7.59	1900.06
6	7.28	726.43	7.22	1232.29	7.76	1149.22	7.63	2022.51
7	7.28	706.64	7.25	1165.63	7.73	1278.19	7.65	1882.24
8	7.28	708.05	7.22	1334.81	7.73	1241.34	7.63	1724.96
9	7.28	705.19	7.22	1247.98	7.72	1239.04	7.62	1943.26
10	7.29	741.85	7.22	1233.39	7.75	1221.86	7.64	1705.27
11	7.28	729.05	7.23	1239.99	7.72	1226.45	7.64	1887.57
12	7.28	699.86	7.25	1188.62	7.7	1236.52	7.62	1933.95
13	7.29	705.15	7.19	1117.89	7.75	1264.92	7.60	1917.42
14	7.27	714.21	7.20	1176.00	7.76	1267.67	7.69	1856.95
15	7.29	671.58	7.23	1231.87	7.74	1264.01	7.62	1965.64
16	7.28	680.45	7.22	1231.46	7.75	1249.07	7.68	1960.91
17	7.30	677.88	7.19	1177.17	7.72	1254.15	7.64	2008.61
18	7.29	698.15	7.22	1056.74	7.75	1208.09	7.69	1805.82
19	7.29	728.30	7.21	1239.91	7.77	1167.84	7.62	1859.78
20	7.31	702.72	7.21	1260.46	7.72	1231.23	7.63	1947.52
21	7.28	716.94	7.22	1190.82	7.71	1269.32	7.61	1933.70
22	7.27	697.23	7.20	1268.26	7.77	1270.57	7.68	1970.46
23	7.28	700.31	7.22	1235.77	7.73	1286.43	7.64	1806.58
24	7.27	701.71	7.22	1155.51	7.74	1179.30	7.62	1750.11
25	7.27	712.15	7.23	1080.59	7.75	1219.54	7.64	1920.89
26	7.28	668.89	7.19	1254.20	7.74	1258.56	7.62	1923.21
27	7.30	754.28	7.18	1082.53	7.74	1260.77	7.68	1921.19
28	7.29	700.32	7.19	1111.60	7.7	1239.94	7.61	1857.66
29	7.30	736.26	7.22	1214.53	7.74	1263.38	7.64	2030.69
30	7.29	699.62	7.21	1214.68	7.74	1251.76	7.63	1935.74

Table XX. 0.3 year strength data.

	Quartz Porcelain		Alumina Porcelain		Glazed Quartz Porcelain		Glazed Alumina Porcelain	
ID#	Thickness (mm)	Force (N)	Thickness (mm)	Force (N)	Thickness (mm)	Force (N)	Thickness (mm)	Force (N)
1	7.29	703.93	7.18	1067.54	7.74	1187.68	7.62	1842.09
2	7.28	680.29	7.23	1038.67	7.72	1207.66	7.65	1923.18
3	7.29	671.36	7.21	1161.89	7.7	1189.94	7.66	1689.96
4	7.29	694.10	7.24	1208.70	7.72	1139.14	7.66	1765.60
5	7.28	720.57	7.22	1204.15	7.71	1140.00	7.66	1801.24
6	7.31	694.36	7.21	1189.72	7.69	1192.83	7.65	1785.22
7	7.29	707.71	7.18	1116.16	7.74	1185.72	7.63	1817.46
8	7.28	694.50	7.19	1142.38	7.71	1197.27	7.65	1765.95
9	7.29	717.13	7.21	1213.86	7.71	1180.94	7.63	1816.47
10	7.27	699.63	7.22	1126.85	7.72	1232.98	7.64	1826.83
11	7.33	723.83	7.17	1175.74	7.76	1153.35	7.64	1734.02
12	7.28	701.32	7.19	1184.73	7.73	1199.25	7.67	1790.37
13	7.27	702.19	7.19	1117.45	7.67	1184.32	7.62	1849.36
14	7.28	688.67	7.18	1032.43	7.73	1199.70	7.67	1825.32
15	7.28	695.51	7.19	1170.43	7.7	1193.71	7.63	1757.64
16	7.31	735.52	7.17	1178.05	7.69	1197.48	7.64	1932.08
17	7.26	688.52	7.20	1096.76	7.74	1239.30	7.61	1859.44
18	7.29	711.47	7.22	1261.26	7.85	1108.09	7.64	1860.50
19	7.30	685.04	7.18	1157.88	7.72	1223.89	7.65	1805.89
20	7.27	643.79	7.18	1196.26	7.71	1168.12	7.66	1890.44